

The Initial Conditions of Clustered Star Formation III. The Deuterium Fractionation of the Ophiuchus B2 Core

R. K. Friesen^{1,2,3}

rfriesen@nrao.edu

J. Di Francesco^{3,2}

P. C. Myers⁴

A. Belloche⁵

Y. L. Shirley⁶

T. L. Bourke⁴

P. André⁷

ABSTRACT

We present N_2D^+ 3-2 (IRAM) and H_2D^+ $1_{11} - 1_{10}$ and N_2H^+ 4-3 (JCMT) maps of the small cluster-forming Ophiuchus B2 Core in the nearby Ophiuchus molecular cloud. In conjunction with previously published N_2H^+ 1-0 observations, the N_2D^+ data reveal the deuterium fractionation in the high density gas across Oph B2. The average deuterium fractionation $R_D = N(\text{N}_2\text{D}^+)/N(\text{N}_2\text{H}^+) \sim 0.03$ over Oph B2, with several small scale R_D peaks and a maximum $R_D = 0.1$. The mean R_D is consistent with previous results in isolated starless and protostellar cores. The column density distributions of both H_2D^+ and N_2D^+ show no correlation with total H_2 column density. We find, however, an anticorrelation in deuterium fractionation with proximity to the embedded

¹National Radio Astronomy Observatory, 520 Edgemont Rd, Charlottesville VA 22903

²Department of Physics and Astronomy, University of Victoria, PO Box 3055, STN CSC, Victoria BC CANADA V8W 3P6

³National Research Council Canada, Herzberg Institute of Astrophysics, 5071 West Saanich Road, Victoria, British Columbia, Canada V9E 2E7

⁴Harvard-Smithsonian Center for Astrophysics, 60 Garden Street, Cambridge, MA 02138

⁵Max-Planck Institut für Radioastronomie, Auf dem Hügel 69, 53121 Bonn, Germany

⁶Steward Observatory, University of Arizona, 933 N. Cherry Ave., Tucson, AZ 85721

⁷Laboratoire AIM, CEA/DSM-CNRS-Université Paris Diderot, IRFU/Service d'Astrophysique, C.E. Saclay, Orme des Merisiers, 91191 Gif-sur-Yvette, France

protostars in Oph B2 to distances $\gtrsim 0.04$ pc. Destruction mechanisms for deuterated molecules require gas temperatures greater than those previously determined through NH_3 observations of Oph B2 to proceed. We present temperatures calculated for the dense core gas through the equating of non-thermal line widths for molecules (i.e., N_2D^+ and H_2D^+) expected to trace the same core regions, but the observed complex line structures in B2 preclude finding a reasonable result in many locations. This method may, however, work well in isolated cores with less complicated velocity structures. Finally, we use R_D and the H_2D^+ column density across Oph B2 to set a lower limit on the ionization fraction across the core, finding a mean $x_{e,lim} \gtrsim few \times 10^{-8}$. Our results show that care must be taken when using deuterated species as a probe of the physical conditions of dense gas in star-forming regions.

Subject headings: ISM: molecules - stars: formation - ISM: kinematics and dynamics - ISM: structure - radio lines: ISM

1. Introduction

The Ophiuchus molecular cloud is a source of ongoing low-mass clustered star formation relatively close to the Sun ($d \sim 120$ pc; Lombardi et al. 2008). Through low resolution DCO^+ observations, Loren et al. (1990) discovered a number of dense Cores (labelled A through F) in the central Ophiuchus region with masses of a few to several tens of solar masses, which represented a range in evolutionary status given the presence or absence of embedded protostars¹. Large-scale submillimetre and millimetre observations of Ophiuchus identified several new Cores, and revealed the Cores were further fragmented into multiple dense clumps, each with masses $M \lesssim 1 M_\odot$ (Motte et al. 1998; Johnstone et al. 2000, 2004; Young et al. 2006; Sadavoy et al. 2010). Analysis of the clump kinematics suggests most are in virial equilibrium and hence not transient objects (André et al. 2007). Recent Spitzer Space Telescope studies of infrared emission towards the Cores have characterized in detail the starless and protostellar clump population (Jørgensen et al. 2008; Enoch et al. 2009). These objects are thus ideal locations to study the physical characteristics of dense cores in the process of forming small stellar clusters.

To characterize the physical properties of the dense, cluster forming Ophiuchus Cores, we have previously studied Oph B, C and F through high resolution NH_3 (1,1) and (2,2) observations (Friesen et al. 2009, hereafter Paper I), and Oph B in both single-dish and interferometer N_2H^+

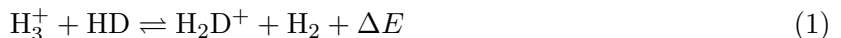
¹In this paper, we describe Oph A, B, C, etc., as ‘Cores’ since this is how these features were named in DCO^+ observations of the L1688 region by Loren et al. (1990). Since then, higher-resolution data such as those described in this paper have revealed substructure in these features that could be themselves precursors to stars, i.e., cores. To avoid confusion, we refer the larger features in Oph as ‘Cores’ and Core substructure identified by CLUMPFIND as ‘clumps’.

1-0 emission (Friesen et al. 2010, hereafter Paper II). The NH_3 and N_2H^+ observations probe gas at densities $n \sim 10^{3-4} \text{ cm}^{-3}$ and $n \sim 10^5 \text{ cm}^{-3}$, respectively.

In Paper I, we identified (through the 3D CLUMPFIND structure-finding algorithm; Williams et al. 1994) a number of individual clumps in NH_3 emission in the Cores, which did not correlate well with those identified in continuum emission. We determined that Oph B and F were warmer on average than typically found for isolated cores (mean $T_K \sim 15 \text{ K}$), and we found no trend with temperatures and H_2 column density calculated from submillimetre continuum emission. In contrast, Oph C is colder, with temperatures decreasing to a minimum of 9 K at the dust continuum emission peak. Line widths in both the Oph B1 and B2 sub-Cores were found to be wide and transonic, despite the presence of three embedded protostars in B2 and none in B1. Oph F, with four embedded protostars, has regions of small and large line widths and complicated line structures. Again similar to isolated objects, NH_3 line widths in Oph C are extremely narrow and consistent with being due to purely thermal motions. In an interesting result, the fractional abundance of NH_3 with respect to H_2 , $X(\text{NH}_3)$, appeared to decrease with increasing H_2 column density, $N(\text{H}_2)$, suggesting NH_3 may be depleted towards locations of high column density and thus may not be tracing the densest core gas. Finally, Paper I revealed that cores with characteristics of both isolated and clustered environments can coexist in a clustered star forming environment.

In Paper II, we again used CLUMPFIND to identify small-scale structure in N_2H^+ emission from Oph B and found that the N_2H^+ clumps matched well NH_3 clumps from Paper I, and were consequently again offset from continuum objects. In both studies, little difference was found in the gas properties towards embedded protostars compared with the general core gas. Line widths in Oph B2 remain large at the densities traced by N_2H^+ . In B1, however, N_2H^+ line widths are significantly narrower than found in NH_3 emission. Applying the gas temperatures determined in Paper I, we found that motions in Oph B1 were subsonic with a mean ratio of non-thermal line width to sound speed $\sigma_{\text{NT}}/c_s = 0.7$ across the core, while in B2 $\sigma_{\text{NT}}/c_s = 1.3$. A clear trend of decreasing $X(\text{N}_2\text{H}^+)$ with increasing $N(\text{H}_2)$ was found towards Oph B2, with emission suggestive of a N_2H^+ hole towards the continuum emission peak found in high resolution N_2H^+ 1-0 emission observed with the Australia Telescope Compact Array.

The results of NH_3 and N_2H^+ observations towards Oph B2 in Paper I and Paper II indicate that the highest density gas may best be probed by molecular emission lines excited at higher critical densities, or by deuterated molecules which are expected to be abundant in cold cores where significant depletion has occurred. In cold molecular cloud cores, the deuteration process is initiated by the reaction



which is exothermic in the forward direction with $\Delta E = 232 \text{ K}$ (Millar et al. 1989). At very low temperatures ($\lesssim 20 \text{ K}$), the forward reaction dominates, making H_2D^+ a key molecular ion in the enhancement of deuterated species in a molecular core. CO, which can destroy both H_2D^+ and

H_3^+ via proton-transfer reactions, is additionally expected to deplete from the gas phase through freeze-out onto dust grains. The deuterium fractionation can thus be elevated orders of magnitude above the cosmic $[\text{D}]/[\text{H}]$ ratio of 10^{-5} for H_3^+ , as well as for other species which react with its deuterated forms.

The ortho- H_2D^+ $1_{11} - 1_{10}$ transition at 372 GHz was first detected towards the low mass young stellar object (YSO) NGC 1333 IRAS 4A by Stark et al. (1999). Multiple detections of H_2D^+ and doubly-deuterated H_3^+ , D_2H^+ , have followed in both starless and protostellar cores (Caselli et al. 2003; Stark et al. 2004; Vastel et al. 2004), including a recent survey of H_2D^+ emission towards sixteen objects by Caselli et al. (2008). Walmsley et al. (2004) show the H_2D^+ abundance determined for the dark core L1544 by Caselli et al. 2003 is consistent with a ‘complete depletion’ model, where heavy elements such as C, N and O (and, consequently, molecules containing these elements) are missing from the gas phase at the highest core densities. In this scenario where no heavy elements are left in the gas phase, H_2D^+ and multiply-deuterated forms of H_3^+ are the only gas tracers of the physical conditions of the dense core.

Based on our previous work in Paper I and Paper II, Oph B2 is a good target to investigate the distribution of deuterated species in a more complex star-forming core. To this end, we present in this paper N_2D^+ 3-2, N_2H^+ 4-3 and H_2D^+ $1_{11} - 1_{10}$ emission maps of Oph B2. In the following sections, we present the observations in §2, and discuss the observed distributions of N_2D^+ 3-2, H_2D^+ $1_{11} - 1_{10}$ and N_2H^+ 4-3 in §3. We fit the observed spectra with a single Gaussian (for H_2D^+) or a multiple-component Gaussian (for N_2D^+ and N_2H^+ due to their hyperfine line structure) and discuss the line velocity centroids and widths in §4, and also present column density and fractional abundance calculations. In §5 we look at the non-thermal line widths in Oph B2 as a function of critical density of the observed emission lines, and discuss trends in the deuterium fractionation. Finally, we present a lower limit to the electron abundance in B2, and summarize our results in §6.

2. Observations

In the following section we discuss the observations presented in this paper. We list the species, transitions, and rest frequencies observed in Table 1.

2.1. N_2D^+ at IRAM

An On-The-Fly (OTF) map of the N_2D^+ 3-2 line at 231.321 GHz in Oph B2 was made at the Institut de Radio Astronomie Millimétrique (IRAM) 30 m Telescope during the 2007 and 2008 winter semesters using the HEterodyne Receiver Array (HERA, Schuster et al. 2004). HERA is a multi-beam spectral line receiver with nine dual polarization pixels arranged in a 3×3 array, with pixels separated by $24''$ [approximately twice the 231 GHz $11''$ beam full width half power (FWHP)]. The maps were performed with the array tracking the sky rotation, and rotated by 9.5° with respect

to the equatorial system, such that the spacing between OTF lines was $4''$. Observations were frequency-switched in-band with a throw of 2×6.9 MHz. The Versatile Spectrometer Assembly (VESPA) autocorrelator was used as the backend, with a 20 MHz bandwidth and 40 kHz channel spacing, corresponding to 0.05 km s^{-1} per channel at 231 GHz.

The data were calibrated to T_A^* units at the telescope using the Multichannel Imaging and Calibration Software for Receiver Arrays (MIRA). Further calibration, including baselining and folding of the frequency-switched spectra, was performed using the CLASS software package². The data were smoothed by two spectral channels along the frequency axis to improve sensitivity, for a final spectral resolution of 80 kHz, or 0.1 km s^{-1} . A second-order polynomial baseline was fitted to the non-line channels and subtracted from the individual spectra before folding the data. The forward (F_{eff}) and beam (B_{eff}) efficiencies of the telescope were interpolated from determined values at 210 GHz and 260 GHz, giving $F_{eff} = 0.92$ and $B_{eff} = 0.58$ at 231 GHz. The data were then calibrated to main beam temperature via the relation $T_{MB} = (F_{eff} / B_{eff}) T_A^*$. For comparison with the N_2H^+ 1-0 results in Paper II, we further converted the data to units of $\text{Jy} / \text{beam}^{-1}$ and convolved the map to a final angular resolution of $18''$ to match the N_2H^+ data.

As the observations were performed in a pooled mode, the $4' \times 3'$ map was observed in three $4' \times 1'$ strips to ensure good sensitivity in potentially limited time. Two-thirds of the map was completed in this manner in winter 2007, while the remaining strip was observed in winter 2008. The sensitivity of the map is consequently not entirely uniform, with the rms noise in the most southern $4' \times 1'$ strip greater [$0.15 \text{ K} (T_{MB})$] than in the rest of the map [$0.08 \text{ K} (T_{MB})$]. Most emission was found in the central and northern map sections, however, so this noise increase does not affect our results significantly.

2.2. H_2D^+ and N_2H^+ at the JCMT

Simultaneous observations of the H_2D^+ $1_{10} - 1_{11}$ and N_2H^+ 4-3 emission lines at 372.421 GHz and 372.673 GHz, respectively, were performed at the James Clerk Maxwell Telescope (JCMT) over the 07A - 08B semesters using the 16-receptor Heterodyne Array Receiver Program B-band receiver (HARP-B, Smith et al. 2008). HARP-B is a 4×4 pixel array, with array spacing of $30''$ and a $2' \times 2'$ footprint. The JCMT beam at 372 GHz is $\sim 13''$ FWHM. We used the ACSIS correlator as the backend, configured to have a 400 MHz effective bandwidth (e.g., wide enough to encompass both lines), tuned halfway in frequency between the two lines, and a frequency resolution of 61 kHz, or 0.05 km s^{-1} at 372.4 GHz. Observations of five separate HARP footprints were performed in position-switching mode to create an undersampled map of H_2D^+ and N_2H^+ over Oph B2. The footprints were placed such that the final beam spacing on the sky is $21''$ with a coverage of $\sim 4' \times 2'$. The fifth footprint provided additional coverage towards the location of peak continuum

²see <http://www.iram.fr/IRAMFR/GILDAS>.

emission in B2, but has lower sensitivity compared with the other footprints. The observations were performed in band 1 weather only ($\tau_{225\text{ GHz}} < 0.05$) and generally while Ophiuchus was above 30° in elevation. The mean rms across the H_2D^+ map is 0.04 K (T_A^*) and 0.05 K (T_A^*) across the N_2H^+ map. The main beam efficiency factors, η_{MB} , of the HARP receptors at 372 GHz are not currently well-known. At 345 GHz, the mean $\eta_{MB} = 0.60$, with an rms variation of $\sim 5\%$ between detectors (Buckle et al. 2009). We therefore estimate $\eta_{MB} \sim 0.6$ with an uncertainty of $\sim 10\%$.

Data reduction was performed using the Starlink software package. Each night’s data were first checked for noisy or malfunctioning pixels, and these pixels were flagged individually for each integration. A linear baseline was then removed from each integration, and the data were combined into a final cube with $15''$ pixels. To increase sensitivity, the data were averaged along the velocity axis by 2 channels, giving a final velocity resolution of 0.1 km s^{-1} .

3. Results

We first discuss the integrated intensity of N_2D^+ 3-2, H_2D^+ 1₁₁ – 1₁₀ and N_2H^+ 4-3 over Oph B2 and compare the species distributions with submillimetre continuum emission and the locations of embedded protostars.

In Figure 1a, we show the integrated N_2D^+ 3-2 intensity (convolved to $18''$ resolution as described in §2.1) in Oph B2 against contours of $850\ \mu\text{m}$ continuum emission observed at the JCMT at $15''$ FWHM resolution (original map by Johnstone et al. 2000, combined with all other SCUBA archive data by Jørgensen et al. 2008, following the description in Kirk et al. 2006). Also identified are the locations of $850\ \mu\text{m}$ continuum clumps (Jørgensen et al. 2008) and Class I protostars [classifications and locations taken from Enoch et al. 2009, two of which were previously identified as Elias 32 and 33 (E32 and E33) by Elias 1978; also VSSG 17 and 18 by Vrba et al. 1975]. The N_2D^+ emission is confined to the northern edge of B2, and generally follows the continuum contours in this region, but a very close correspondence is only seen towards the north-east tip of B2. Three maxima of integrated intensity are present, of which two are co-located with continuum clumps, while the third is seen to the north-west of the continuum peak. The N_2D^+ emission is weak towards the continuum emission peak, and avoids entirely areas near the protostars.

In Figure 1b, we plot the N_2D^+ 3-2 integrated intensity contours over a map of N_2H^+ 1-0 integrated intensity, observed with the Nobeyama 45 m Telescope at $18''$ resolution. The N_2H^+ observations and analysis were presented in Paper II. We also show the locations of N_2H^+ clumps, identified through CLUMPFIND in Paper II. Overall, N_2D^+ emission is found within the extent of N_2H^+ 1-0 emission. In a similar fashion to the continuum emission, however, we find offsets between the locations of peak N_2D^+ and N_2H^+ integrated intensity. In particular, the N_2D^+ integrated intensity maximum is offset from the integrated N_2H^+ 1-0 maximum in B2 by $\sim 20''$ to the northeast, ~ 1 beam width. The N_2H^+ 1-0 integrated intensity maximum is itself offset to the east from the continuum peak by $\sim 22''$ (Paper II). The northeastern N_2D^+ integrated intensity

peak, which corresponds well with continuum contours, is also offset from the integrated N_2H^+ intensity peak by $\sim 20''$ to the east.

We show in Figure 2 H_2D^+ $1_{11} - 1_{10}$ spectra across Oph B2 with overlaid $850\ \mu\text{m}$ continuum contours. We find that significant H_2D^+ emission is present over much of Oph B2, with a larger extent than found in H_2D^+ observations towards any other cores so far observed (Caselli et al. 2003; Vastel et al. 2006; Pagani et al. 2009). The H_2D^+ emission again follows generally the continuum emission but avoids the embedded protostars in B2, similar to N_2D^+ . While relatively strong emission is seen towards the continuum peak, the H_2D^+ integrated intensity maximum (not shown) is also offset the continuum peak by an estimated $\sim 20 - 30''$ (due to the map’s undersampling we are unable to determine exactly the location of maximum integrated intensity). In contrast to the N_2D^+ emission, the H_2D^+ integrated intensity maximum is found to the northwest rather than the northeast (although N_2D^+ emission is also found towards the H_2D^+ peak). The pixel-to-pixel variations seen in Oph B2 may not be significant, however, due to the $\sim 5\%$ variation determined for the main beam efficiency factors between different HARP receptors (Buckle et al. 2009). We detect some H_2D^+ emission in north-east B2 where was found strong N_2D^+ emission, but do not see a significant integrated intensity maximum. (Note, however, that the HARP footprints do not extend past an R.A. of 16:27:35, and are therefore not sensitive to any emission at the tip of the continuum contours in this region.) Overall, where N_2D^+ emission appears strongest in the north and east of Oph B2, H_2D^+ emission is strongest towards B2’s western edge.

In Figure 3, we show N_2H^+ $4-3$ spectra across Oph B2 with overlaid $850\ \mu\text{m}$ continuum emission contours. We find bright N_2H^+ $4-3$ emission over most of B2. The greatest integrated N_2H^+ $4-3$ intensity (not shown) is found towards E33, while additional strong N_2H^+ $4-3$ emission is found towards E32 and the $850\ \mu\text{m}$ continuum emission peak. A separate integrated intensity peak is found in northeast B2 (where we also find strong N_2D^+ $3-2$ emission). Overall, while the N_2H^+ $4-3$ emission is generally confined to areas where there is also continuum emission, the strongest N_2H^+ $4-3$ emission is found away from the brightest continuum contours. A comparison between Figure 3 and the N_2H^+ $1-0$ integrated intensity in Figure 1b (greyscale) reveals a significant discrepancy between the locations of strong N_2H^+ $1-0$ and $4-3$ emission in Oph B. We probe the possible causes of the offset, including the excitation and opacity of the lines, further below.

4. Analysis

4.1. Line fitting

The rotational transitions of the linear molecular ions N_2H^+ and N_2D^+ contain hyperfine structure, which is dominated by the interactions between the molecular electric field gradient and the electric quadrupole moments of the two nitrogen nuclei (Dore et al. 2004). Rotational transitions at higher J contain greater numbers of hyperfine components at smaller frequency intervals, i.e., the satellite components are found more closely spaced and can overlap significantly.

In particular, the N_2H^+ 4-3 and the N_2D^+ 3-2 transitions contain 21 and 25 hyperfine components, respectively, with relative line strengths $\gtrsim 0.001$ (Pagani et al. 2009; Gerin et al. 2001).

For N_2H^+ 4-3, we calculate the relative line strengths $s_{J F_1 F \rightarrow J' F'_1 F'}$ from the Einstein A coefficients $A_{J F_1 F \rightarrow J' F'_1 F'}$ and frequencies $\nu_{J F_1 F \rightarrow J' F'_1 F'}$ given by Pagani et al. (2009), using

$$A_{J F_1 F \rightarrow J' F'_1 F'} = \frac{64\pi^4}{3hc^2} \mu^2 \nu_{J F_1 F \rightarrow J' F'_1 F'}^3 \frac{J}{[F]} s_{J F_1 F \rightarrow J' F'_1 F'} \quad (2)$$

where $\mu = 3.4\text{D}$ is the permanent electric dipole moment, J is the upper rotational quantum number and $[F] = 2F + 1$ accounts for the degeneracy of the hyperfine states. For the N_2H^+ 4-3 transition, fourteen components at 8 distinct frequencies make up the main centroid emission, and lie within 0.4 km s^{-1} of each other. At low optical depths the line profile does not differ substantially from a Gaussian profile, while the relative intensities of the satellite lines to the main line component remain small even at large opacities ($\sim 20\%$ at $\tau \sim 10$). Nevertheless, the satellite components of the line are visible towards several pixels in Oph B (identified as locations A through C on Figure 3), largely near the embedded protostar E33. In some locations the line structure is confused with a significant blue emission shoulder, which is not due to any hyperfine structure, but which may be associated with an outflow stemming from either E33 or E32 (Kamazaki et al. 2003, White *et al.* 2010, in preparation). We were thus able to fit well the hyperfine structure towards only one location in the map, and constrain the excitation temperature, T_{ex} , and opacity, τ , towards two others.

We fit the hyperfine structure with a custom Gaussian hyperfine structure fitting routine written in IDL, described in detail in Paper I, assuming equal excitation temperatures T_{ex} for each hyperfine component. The line fitting routine does not take into account the significant overlap between hyperfine components in both the N_2H^+ and N_2D^+ transitions, but we find the total N_2H^+ line opacities are still small where the satellite structure is seen ($\tau \sim 2 - 3$) and we therefore do not expect line overlap to introduce substantial errors.

At low opacities, we cannot solve for τ and T_{ex} independently. Given a reasonable estimate for T_{ex} , however, we may attempt to fit the line without visible satellite structure. In Paper II, we determined T_{ex} for N_2H^+ 1-0 emission across Oph B, and to first order can expect the same T_{ex} to describe the excitation of all rotational levels of N_2H^+ . This assumption was found to be accurate in a recent study of N_2H^+ and N_2D^+ emission in L1544, where Caselli et al. (2002b) were able to determine separately the excitation temperatures for N_2H^+ 1-0, 3-2 and N_2D^+ 2-1 and 3-2, and found they were consistent within uncertainties. We find, however, that while most of the data can be fit reasonably well using the N_2H^+ 1-0 T_{ex} values, visual inspection showed that a simple Gaussian fit the data equally well, or significantly better, in many cases, and the line opacities were not well-constrained.

Because multiple components of similar line strength overlap to form the main N_2H^+ 4-3 component, a Gaussian fit will overestimate the line width, while the returned v_{LSR} will be shifted

relative to a full HFS fit. The shift in v_{LSR} can be corrected ($\Delta v_{LSR} = 0.036 \text{ km s}^{-1}$), and at low opacities, the increase in Δv is small ($\lesssim 10\%$ for $\tau < 1$, up to $\sim 25\%$ for $\tau \sim 2$). In the following sections, we thus discuss only the results of the Gaussian fitting of the N_2H^+ 4-3 emission unless otherwise stated.

No hyperfine structure was seen above the rms noise in N_2D^+ 3-2 emission across Oph B. We are therefore unable to fit well the N_2D^+ 3-2 hyperfine structure solving for both τ and T_{ex} . Here, however, equating the N_2D^+ T_{ex} with that found for N_2H^+ 1-0 emission resulted in better constraints on the opacity. The hyperfine fit, using the relative component strengths and velocities from Gerin et al. (2001), is thus more informative than a simple Gaussian fit, and we discuss the results from the full HFS fit in the following sections.

To properly calculate the line width, Δv , we subtracted in quadrature the resolution width, Δv_{res} (0.1 km s^{-1} for all species), from the observed line width, Δv_{obs} , such that $\Delta v = \sqrt{\Delta v_{obs}^2 - \Delta v_{res}^2}$. The uncertainties reported in the returned parameters are those determined by the fitting routine, and do not take the calibration uncertainty into account. The calibration uncertainty does not affect the uncertainties returned for v_{LSR} or Δv . The excitation temperature, column densities and fractional abundances discussed further below, however, are dependent on the amplitude of the line emission, and are thus affected by the absolute calibration uncertainty.

The H_2D^+ $1_{11} - 1_{10}$ emission line has no hyperfine structure. We consequently fit the emission at each pixel with a single Gaussian (again in IDL) to determine the line amplitude, v_{LSR} and Δv across Oph B2.

4.2. Centroid velocity and line widths

Table 2 lists the mean, rms, minimum and maximum values of v_{LSR} and Δv for N_2H^+ 4-3, N_2D^+ 3-2, and H_2D^+ $1_{11} - 1_{10}$, along with the same results from NH_3 (1,1) and N_2H^+ 1-0 presented in Paper I and Paper II for comparison.

We show in Figure 5 the N_2D^+ v_{LSR} and Δv over Oph B2. We only plot values where the S/N ratio of the peak line intensity was ≥ 5 . The mean v_{LSR} across B2 is 4.02 km s^{-1} with an rms variation of 0.19 km s^{-1} . Lower v_{LSR} values are found towards the western and northeastern regions of the Core, with the maximum $v_{LSR} = 4.44 \text{ km s}^{-1}$ in the east towards the NH_3 (1,1) clump B2-A7 (identified in Paper I and labelled on Figure 5; coincident with the N_2H^+ 1-0 clump B2-N6 from Paper II). The variation in v_{LSR} does not suggest global rotation of B2. The N_2D^+ line velocities shift between 3.7 km s^{-1} and 4.4 km s^{-1} over $\sim 40''$, or $\sim 4800 \text{ AU}$, to the west of E32. Nearby, the line v_{LSR} shifts from 3.7 km s^{-1} to 4.2 km s^{-1} on either side of the western embedded protostar.

The mean N_2D^+ 3-2 line width $\Delta v = 0.53 \text{ km s}^{-1}$ with an rms variation of 0.20 km s^{-1} . In general, the widest line widths are found near E32 and the western protostar (Oph-emb5, Enoch et al. 2009), to a maximum $\Delta v = 1.36 \text{ km s}^{-1}$ in western B2 (but note the largest Δv values are found

only $\sim 45''$ to the northwest of some of the narrowest Δv values). The locations of large line widths correspond well with the locations of dramatic v_{lsr} shifts, described above. Away from the protostars, only small variations in the relatively narrow line widths are seen, notably towards the northeast and southwest, with $\Delta v \sim 0.3 \text{ km s}^{-1}$. Two objects are associated with localized narrow Δv . An $850 \mu\text{m}$ continuum clump (162725-24273, Jørgensen et al. 2008), shown on the image, was identified where the southwestern narrow line widths are found. In the east, B2-A7 NH_3 is also associated with a Δv minimum of 0.36 km s^{-1} . This is similar to the clump line width in N_2H^+ 1-0 emission at $18''$ resolution, but nearly a factor of two larger than found in N_2H^+ 1-0 interferometer observations of the clump presented in Paper II.

In Figure 6a and Figure 6c we show the v_{LSR} determined through Gaussian fitting of the H_2D^+ $1_{11} - 1_{10}$ and N_2H^+ 4-3 lines, respectively. Visual inspection of the v_{LSR} values shows that the H_2D^+ emission is similar kinematically to the N_2D^+ 3-2 values in Figure 5a, while a small shift in v_{LSR} of $\sim +0.2 \text{ km s}^{-1}$ is seen in N_2H^+ 4-3 emission towards Elias 32 and the $850 \mu\text{m}$ continuum emission peak and co-located $850 \mu\text{m}$ continuum emission peak (co-located with the continuum clump B2-MM8). The shift is small but significant given the otherwise excellent agreement in v_{LSR} between the different tracers over B2 (see Table 2).

We show in Figure 6b and Figure 6d the Δv of the H_2D^+ and N_2H^+ lines. The H_2D^+ line widths are large, with a mean $\Delta v = 0.74 \text{ km s}^{-1}$, and do not vary greatly over Oph B2 (Δv rms = 0.19 km s^{-1}). Slightly greater line widths are found in the western half of B2. Gaussian fits to the N_2H^+ 4-3 data find the lines are slightly more narrow, with a mean $\Delta v = 0.69 \text{ km s}^{-1}$. As noted in §4.1, Gaussian fits likely overestimate the true N_2H^+ line width by $\sim 10 - 25\%$. Wider N_2H^+ lines are also found towards western Oph B2, while narrower lines are seen towards the submillimetre continuum emission peak and in B2’s eastern half. N_2H^+ lines of average width are found towards the embedded protostars, but become wider at pixels directly offset from the infrared sources. In particular, directly to the east of E32 and E33, the N_2H^+ 4-3 line profiles show a significant blue shoulder with emission extending to $v_{\text{LSR}} \sim 2.5 \text{ km s}^{-1}$. Figure 4c shows the result of a two-component Gaussian fit to the line and blue shoulder at location C in Figure 3.

4.3. N_2H^+ opacity and excitation temperature

Comparison of the N_2H^+ 1-0 and 4-3 line emission (see Figure 1b and Figure 3) shows that while in both cases emission is found over much of Oph B2, the integrated intensity distributions of the two transitions are quite different. It is thus unclear whether the excitation conditions for both transitions would be equal.

Towards several pixels, hyperfine structure is visible. These locations are labeled A through C on Figure 3, and these spectra are again shown in Figure 4. Using the full hyperfine component fit (overlaid on the spectrum), we were able to determine reasonably well the excitation temperature and opacity of the N_2H^+ 4-3 line, $T_{ex,4-3}$ and τ_{4-3} towards location A, with the resulting best fit

total line opacity $\tau_{4-3} = 2.5 \pm 1$, with $T_{ex,4-3} = 8 \pm 1$ K. Both $T_{ex,4-3}$ and τ_{4-3} are approximately consistent with values found in Paper II for N_2H^+ 1-0 emission at the same location, where $T_{ex,1-0} = 7.3 \pm 0.1$ K and $\tau_{1-0} = 3.1 \pm 0.6$. The brightest N_2H^+ 4-3 line emission, however, and additionally the maximum integrated intensity, is located towards E33 (location B in Figure 3, directly south of A). The intensity ratio of the main N_2H^+ 4-3 component with an apparent red satellite (line strength only $2\times$ the data rms noise level, but at the correct velocity and with a width that matches the main component, see Figure 4b) suggests that the N_2H^+ 4-3 opacity towards E33 remains moderately optically thick, $\tau_{4-3} \sim 3$, and the corresponding $T_{ex,4-3} \sim 8$. The expected line profile given these values is overlaid on the spectrum in Figure 4. The integrated N_2H^+ 1-0 emission decreases significantly towards E33 (see Figure 1b and Paper II). Additionally, the emission is confused by multiple velocity components which preclude robust fits to the 1-0 spectra, so we do not have a good estimate of the N_2H^+ 1-0 T_{ex} at this location. At location D in Figure 3, satellite emission is again seen, but here the hyperfine fits are confused by significant blue shoulder emission. The best-fit results give $T_{ex} \sim 7.5$ K – 10 K, with $\tau \sim 1 - 3$. We overlay the expected line profile for $T_{ex} = 8.5$ K and $\tau = 2$ on spectrum D in Figure 4. Elsewhere, no hyperfine structure is visible in the N_2H^+ 4-3 line.

For opacity ratios between the N_2H^+ 4-3 and N_2H^+ 1-0 lines, $\tau_{4-3}/\tau_{1-0} \sim 0.3$ and similar line widths, the derived N_2H^+ column density, $N(\text{N}_2\text{H}^+)$, calculated using either transition following Caselli et al. (2002c) (Equation A1), is equal if both $T_{ex,1-0}$ and $T_{ex,4-3} \sim 7$ K. At lower opacity ratios, the required T_{ex} also decreases. On average, the N_2H^+ 1-0 and 4-3 line widths agree, however we note that since we cannot fit well the hyperfine structure, the N_2H^+ 4-3 widths are an overestimate of the true value by $\sim 10 - 25\%$. This uncertainty propagates linearly into the column density calculation. With this caveat, an excitation temperature $T_{ex} \sim 7$ K agrees well with the mean T_{ex} determined from HFS fitting of the N_2H^+ 1-0 line in Paper II. We have no column density estimate towards E33 from N_2H^+ 1-0 emission. Near E32 and E33, however, the greater relative N_2H^+ 4-3 opacity requires either a higher common $T_{ex} \sim 10 - 11$ K to obtain similar $N(\text{N}_2\text{H}^+)$ estimates, which does not agree with our N_2H^+ 1-0 T_{ex} measurement, or the excitation of the N_2H^+ 4-3 line must be greater than that of the 1-0 line by $\sim 2 - 3$ K. This moderate increase in excitation temperature of the higher excitation N_2H^+ line is not ruled out by our data. Detailed modeling of the N_2H^+ emission near the embedded protostars using radiative transfer codes would help disentangle the excitation and opacity effects.

4.4. Column density and fractional abundance

We next discuss the column densities of N_2D^+ and H_2D^+ derived from the observed line emission. The N_2H^+ column density was calculated in Paper II.

4.4.1. N_2D^+

We calculate the total N_2D^+ column density, $N_{tot}(N_2D^+)$, from the integrated intensity of the 3-2 transition following Caselli et al. (2002a) for optically thin emission:

$$N_{tot} = \frac{8\pi W}{\lambda^3 A} \frac{g_u}{g_l} \frac{1}{J_\nu(T_{ex}) - J_\nu(T_{bg})} \frac{1}{1 - \exp(-h\nu/kT_{ex})} \frac{Q_{rot}(T_{ex})}{g_l \exp(-E_l/kT_{ex})} \quad (3)$$

where W is the line integrated intensity, A is the Einstein spontaneous emission coefficient, g_u and g_l are the statistical weights of the upper and lower states, respectively, and the equivalent Rayleigh-Jeans excitation and background temperatures are given by $J_\nu(T_{ex})$ and $J_\nu(T_{bg})$. The rotational energy $E_J = J(J+1)hB$ for linear molecules, where the rotation quantum number $J = 2$ for the lower energy state and $B = 38554.717$ MHz is the rotational constant (Sastry et al. 1981). The partition function $Q_{rot}(T_{ex}) = \sum_{J=0}^{\infty} (2J+1) \exp(-E_J/kT_{ex})$, and we use the integrated value, $Q_{rot}(T_{ex}) = kT_{ex}/(hB) + 1/3$. We assume that the excitation temperature T_{ex} is the same for all rotational levels, and use the fitted N_2H^+ 1-0 T_{ex} from Paper II as an estimate of the excitation temperature of the N_2D^+ line at each pixel (as discussed in §4.1). All other parameters remaining equal, at the average T_{ex} of the N_2H^+ 1-0 line, a decrease in T_{ex} by 2 K would increase the resulting N_2D^+ column density by a factor $\lesssim 2$, while an increase in T_{ex} by 2 K would decrease the resulting N_2D^+ column density by $\lesssim 0.5$. We show $N(N_2D^+)$ across Oph B2 in Figure 7a.

We then calculate the fractional N_2D^+ abundance per pixel,

$$X(N_2D^+) = N(N_2D^+)/N(H_2) \quad (4)$$

where the H_2 column density, $N(H_2)$, is calculated from $850 \mu\text{m}$ continuum emission. The $15''$ data were convolved to a final $18''$ FWHM resolution to match the convolved N_2D^+ data. The H_2 column density is then given by $N(H_2) = S_\nu / [\Omega_m \mu m_H \kappa_\nu B_\nu(T_d)]$, where S_ν is the $850 \mu\text{m}$ flux density, Ω_m is the main-beam solid angle, $\mu = 2.33$ is the mean molecular weight, m_H is the mass of hydrogen, κ_ν is the dust opacity per unit mass at $850 \mu\text{m}$, where we take $\kappa_\nu = 0.018 \text{ cm}^2 \text{ g}^{-1}$, and $B_\nu(T_d)$ is the Planck function at the dust temperature, T_d . As in Paper I and Paper II, we expect the gas and dust to be well-coupled in Oph B2, and set $T_d = T_K$, the gas kinetic temperature determined from NH_3 (1,1) and (2,2) inversion line ratios. We refer the reader to the detailed discussion of the uncertainties in the $N(H_2)$ values presented in Paper II, but note that the derived H_2 column densities have uncertainties of factors of a few. Additionally, due to the negative artifacts introduced into the data from the observational chopping technique (again discussed in detail in Paper II), we limit the analysis to pixels where $S_\nu \geq 0.1 \text{ Jy beam}^{-1}$, though the rms noise level of the continuum map is $\sim 0.03 \text{ Jy beam}^{-1}$. For a dust temperature $T_d = 15 \text{ K}$, this flux level corresponds to $N(H_2) \sim 6 \times 10^{21} \text{ cm}^{-2}$.

The column density distribution is not similar to the the integrated intensity map shown in Figure 1a. Figure 7a shows several small peaks of $N(N_2D^+)$ in B2 which largely correspond with

local minima in the excitation temperature ($T_{ex} \sim 5$ K compared with the mean $T_{ex} \sim 7$ K, where the uncertainty in T_{ex} is $\sim 0.4 - 0.6$ K). The $N(\text{N}_2\text{D}^+)$ peaks remain within the continuum contours but avoid maxima of continuum emission. We find a mean $N(\text{N}_2\text{D}^+) = 1.8 \times 10^{11} \text{ cm}^{-2}$ in Oph B2 with an rms variation of $1.3 \times 10^{11} \text{ cm}^{-2}$. The maximum $N(\text{N}_2\text{D}^+) = 7.1 \times 10^{11} \text{ cm}^{-2}$ is found towards the northeast. If we calculate $N(\text{N}_2\text{D}^+)$ assuming a constant $T_{ex} = 7$ K, the distribution follows the integrated intensity but the mean value and variation remain the same.

The fractional N_2D^+ abundance (not shown) follows a similar distribution to the N_2D^+ column density. We find a mean $X(\text{N}_2\text{D}^+) = 8.2 \times 10^{-12}$ with an rms variation of 5.1×10^{-12} . The maximum $X(\text{N}_2\text{D}^+) = 2.9 \times 10^{-11}$ is again found towards northeast Oph B2. Within the continuum emission contours, the lowest *measured* N_2D^+ abundances ($X(\text{N}_2\text{D}^+) \sim 2 \times 10^{-12}$) are found towards the continuum emission peak and B2-MM8 clump (emission towards the Elias 33 protostar was not above our S/N limit for analysis).

4.4.2. H_2D^+

To calculate the H_2D^+ column density, $N(\text{H}_2\text{D}^+)$, we first estimate the line opacity τ from the $\text{H}_2\text{D}^+ 1_{11} - 1_{10}$ line emission using

$$\tau = -\ln \left[1 - \frac{T_{MB}}{J(T_{ex}) - J(T_{bg})} \right] \quad (5)$$

where we must assume a priori an excitation temperature T_{ex} for the transition. An upper limit is given by the gas kinetic temperature T_K . For the pixels where the H_2D^+ S/N ratio > 5 , we found in Paper I a mean $T_K = 14.5$ K with an rms variation of 1.1 K (slightly less than the mean $T_K = 15$ K found for the entire Oph B Core in Paper I), with a minimum $T_K \lesssim 13$ K towards the highest $N(\text{H}_2)$ values. We note, however, that the critical density at which NH_3 is excited ($n_{cr} \sim 10^{3-4} \text{ cm}^{-3}$) is lower than that of the H_2D^+ transition by an order of magnitude, and the NH_3 temperatures, or the variation in T_K , may not accurately reflect the conditions where H_2D^+ is excited.

In their recent H_2D^+ study of several starless and protostellar cores, Caselli et al. (2008) found that the $\text{H}_2\text{D}^+ T_{ex}$ was similar to or slightly less than the core T_K values, which were estimated through a variety of methods (e.g., continuum observations, NH_3 inversion observations as for B2, and multiple transition observations of molecules such as HCO^+). Six of the seven protostellar cores in their sample had excitation temperatures which ranged from 9 K to 14 K and similar densities to those calculated for B2 in Paper II. Based on these values, and to better compare our results with Caselli et al., we use a constant excitation temperature $T_{ex} = 12$ K in Equation 5. Given $T_{ex} = 12$ K, we find a mean $\tau = 0.13$, with a minimum $\tau = 0.05$ and maximum $\tau = 0.28$, which agree well with the Caselli et al. results in protostellar cores.

The total column density of ortho-H₂D⁺ is then given by Vastel et al. (2006)

$$N(\text{ortho-H}_2\text{D}^+) = \frac{8\pi}{\lambda^3 A_{ul}} \frac{Q_{rot}(T_{ex})}{g_u} \frac{\exp(E_u/kT_{ex})}{\exp(h\nu/kT_{ex}) - 1} \int \tau dv \quad (6)$$

where $g_u = 9$, $E_u/k = 17.8$ K, and $A_{ul} = 1.08 \times 10^{-4} \text{ s}^{-1}$ for the $1_{11}-1_{10}$ transition (Ramanlal & Tennyson 2004). The integral $\int \tau dv = \frac{1}{2} \sqrt{\pi/(\ln(2))} \tau \Delta v$. We calculate Q_{rot} by reducing the H₂D⁺ level structure to a 2-level system following Caselli et al. Since the energy of the first excited state above ground is $E/k = 17.8$ K and that of the second excited state is $E/k = 110$ K, we expect this approximation to be valid in Oph B2 given the low temperatures determined in Paper I. The partition function depends on T_{ex} , which we have estimated to be 12 K. In Figure 8, we plot the variation in τ , Q_{rot} and $N(\text{ortho-H}_2\text{D}^+)$ with T_{ex} given a line $T_{MB} = 0.5$ K and $\Delta v = 0.7 \text{ km s}^{-1}$ (typical values in B2), and have listed the returned values for T_{ex} between 7 K and 15 K in Table 3. While the variation in returned parameters is fairly large with small T_{ex} changes at low T_{ex} values (i.e., factors ~ 2 or more around $T_{ex} \sim 7$ K), at higher T_{ex} the values vary less. For example, an increased $T_{ex} = 14$ K rather than $T_{ex} = 12$ K would result in a decreased $N(\text{ortho-H}_2\text{D}^+)$ by $\sim 20\%$, while a decreased $T_{ex} = 10$ K would result in an increased $N(\text{ortho-H}_2\text{D}^+)$ by $\sim 30\%$. We thus assume an uncertainty of $\sim 25\%$ in the $N(\text{H}_2\text{D}^+)$ values reported here.

To calculate the total H₂D⁺ column density in B2, an estimate of the ortho- to para-H₂D⁺ (o/p-H₂D⁺) ratio is needed. The ground state para-H₂D⁺ transition occurs at a frequency of 1.37 THz; this line is difficult to observe from the ground and may not be excited at the low temperatures found in star-forming cores. Without a direct measurement of the population of the para state, we look to chemical models to predict the o/p-H₂D⁺ ratio, which show that the o/p-H₂D⁺ ratio is directly dependent on o/p-H₂. Walmsley et al. (2004) find that the o/p-H₂ ratio increases to a steady-state value of $\sim 5 \times 10^{-4}$ at $T = 10$ K and $n = 10^6 \text{ cm}^{-3}$, similar to the density and temperature determined for Oph B2 in Paper I and Paper II. The same models predict o/p-H₂D⁺ $\sim 0.2 - 0.3$. Using Bonnor-Ebert sphere core models, Sipilä et al. (2010) also predict o/p-H₂D⁺ ratios $\lesssim 0.5$ at $T \sim 10 - 15$ K in steady-state. Their models show that the o/p-H₂D⁺ ratio can dramatically increase to values $\sim 2 - 3$ at $T \lesssim 10$ K, but these temperatures are unlikely based on our analysis of Oph B2.

It is not clear, however, whether steady-state models accurately represent conditions in star forming cores like B2. The dynamical timescale of a collapsing core can be much shorter than some of the chemical timescales, leading to large departures of free-fall model predictions from steady-state models (Flower et al. 2006). For example, Flower et al. show that the steady-state model underpredicts the o/p ratio by up to an order of magnitude compared with a free-fall collapse model at gas densities $n \lesssim 10^6 \text{ cm}^{-3}$ (the models are more consistent at higher densities). Consequently, it may not be unreasonable to expect variations in the o/p-H₂D⁺ ratio across B2 as it evolves. Given this uncertainty in the o/p-H₂D⁺ ratio, we limit discussion to $N(\text{ortho-H}_2\text{D}^+)$, but note that the total $N(\text{H}_2\text{D}^+)$ is likely greater than $N(\text{ortho-H}_2\text{D}^+)$ by a factor of a few.

We show in Figure 9 the resulting $N(\text{ortho-H}_2\text{D}^+)$ distribution across Oph B2. Including only pixels where the $S/N > 5$, we find the mean $N(\text{ortho-H}_2\text{D}^+) = 1.4 \times 10^{13} \text{ cm}^{-2}$ with an rms variation of $0.7 \times 10^{13} \text{ cm}^{-2}$ over Oph B2. To this sensitivity limit, we find a minimum $N(\text{ortho-H}_2\text{D}^+) = 4.1 \times 10^{12} \text{ cm}^{-2}$. The maximum $N(\text{ortho-H}_2\text{D}^+) = 3.3 \times 10^{13} \text{ cm}^{-2}$ is found $\sim 30''$ to the northwest of the $850 \mu\text{m}$ continuum peak. The largest $\text{ortho-H}_2\text{D}^+$ column densities are found in the western half of Oph B2, with moderate $N(\text{ortho-H}_2\text{D}^+)$ values extending to the northeast.

We next calculate $X(\text{ortho-H}_2\text{D}^+)$ as described for N_2D^+ above, and show in Figure 9b the $X(\text{ortho-H}_2\text{D}^+)$ distribution across B2. Similarly to the column density distribution, the largest H_2D^+ abundances, $X(\text{ortho-H}_2\text{D}^+) \sim 4 - 5 \times 10^{-10}$, are found in the west. A local $X(\text{ortho-H}_2\text{D}^+)$ minimum of $\sim 2 \times 10^{-10}$ is found towards the central continuum emission peak, with similar abundances towards the northeast.

4.5. Using H_2D^+ , N_2H^+ and N_2D^+ to determine T_K

The molecular weight of H_2D^+ ($m_{mol} = 4.01 m_H$) is much less than that of N_2H^+ or N_2D^+ ($29.01 m_H$ and $30.02 m_H$, respectively). If we assume that the H_2D^+ $1_{11} - 1_{10}$, N_2H^+ $4-3$ or N_2D^+ $3-2$ transitions are excited in the same environment within Oph B2, we would expect each to trace the same core motions, and be described by the same kinetic temperature T_K . This collocation would imply that the non-thermal line widths for the two species should be equal, where $\sigma_{NT}^2 = \sigma_{obs}^2 - \sigma_{th}^2$. Given equal T_K , the H_2D^+ thermal line width, $\sigma_{th} = (kT_k/m_{mol})^{1/2}$, will be measurably larger than that of N_2H^+ due to its smaller molecular weight. At $T_K = 12 \text{ K}$, for example, $\sigma_{th} = 0.06 \text{ km s}^{-1}$ for N_2D^+ and 0.16 km s^{-1} for H_2D^+ . We can use this difference in thermal line widths to determine the kinetic gas temperature by equating the non-thermal line widths and solving for T_K (e.g., in the case of N_2H^+):

$$T_K = \frac{1}{k_B} \left(\frac{1}{m_{\text{H}_2\text{D}^+}} - \frac{1}{m_{\text{N}_2\text{H}^+}} \right)^{-1} [\sigma_{obs}^2(\text{H}_2\text{D}^+) - \sigma_{obs}^2(\text{N}_2\text{H}^+)] \quad (7)$$

Mean temperatures of $9.2 \pm 0.2 \text{ K}$, in good agreement with temperatures derived from NH_3 alone, were derived in this manner towards a number of dense cores by Fuller & Myers (1993) using the molecular species HC_3N and NH_3 . The largest source of error in the derived T_K likely arises from the assumptions listed above rather than from the propagation of the small uncertainties on the observed line widths.

Overall, we expect the comparison of H_2D^+ and N_2D^+ to be most accurate, given the similar critical densities of the transitions, the fact that N_2D^+ must form from H_2D^+ , and the similar distribution of integrated intensity (in contrast with the poor correlation between H_2D^+ and N_2H^+ $4-3$ emission; see Figures 1a and 2). The different distributions of H_2D^+ and N_2H^+ $4-3$ in Oph B2 suggest that these two species are not excited in the same environment in the core. Additionally,

since our estimates of the N_2H^+ line widths are not accurate (given the unresolved hyperfine structure), we will focus only on N_2D^+ for this analysis.

We show in Figure 10 the temperatures calculated based on Equation 7 for H_2D^+ and N_2D^+ 3-2. Only pixels where the signal-to-noise ratio of both lines was > 5 are shown. The derived T_K values span a large range, from unphysical negative values (~ -11 K) to unrealistically large values (~ 75 K). Using the mean Δv values of H_2D^+ and N_2D^+ from Table 2, we calculate a mean $T_K = 16$ K, similar to that determined through NH_3 analysis. Multiple pixels with $T_K \sim 12$ K are found surrounding the central continuum emission peak. Negative temperatures, however, are found associated with the continuum peak and associated clump B2-MM8.

From Equation 7, we calculate negative T_K values when the observed H_2D^+ line widths are less than those of N_2D^+ 3-2. We show in Figure 11 (bottom) Δv derived for H_2D^+ and N_2D^+ emission (data values in $15''$ pixels plotted), along with the spectra and relative fits towards B2-MM8 (top). Over most of B2, N_2D^+ line widths are narrower than H_2D^+ , and thus $T_K > 0$ K. The negative temperatures derive from two adjacent pixels towards B2-MM8 where the N_2D^+ $\Delta v > \Delta v$ of H_2D^+ . Figure 11 shows non-Gaussianity in the spectra of both species towards B2-MM8, which complicates the calculation of a single line width to describe the emission.

Why would we find greater N_2D^+ Δv than H_2D^+ Δv only towards the central continuum peak? One possibility is suggested by the spectra in Figure 11, where additional emission in the H_2D^+ spectrum is clearly seen blue-shifted relative to the main Gaussian peak. For the H_2D^+ line, the best-fit Gaussian does not include the blue line shoulder. Slight blue asymmetry is also visible in the N_2D^+ line, but the distinction between the main component and the shoulder is less obvious. It is possible that the shoulder emission of N_2D^+ 3-2 is spread over a larger range in v_{LSR} due to the contribution of multiple hyperfine components to the observed emission (which would each contain emission at the central line velocity and at the shoulder velocity), broadening the line overall. The best fit to the N_2D^+ line thus cannot distinguish well between the main and shoulder emission, resulting in an artificially broad Δv .

5. Discussion

5.1. Line widths and density

The mean line widths listed in Table 2 show that on average, the observed Δv for a given molecular line decreases with increasing critical line density, suggesting that the gas in B2 becomes more quiescent at higher densities (omitting N_2H^+ 4-3, where Δv is an overestimate). For an average gas temperature $T_K = 15$ K, the resulting non-thermal line contribution decreases from $\sigma_{\text{NT}} = 0.36 \text{ km s}^{-1}$ for NH_3 (1,1) emission to $\sigma_{\text{NT}} = 0.22 \text{ km s}^{-1}$ for N_2D^+ 3-2 emission (for $n_{\text{cr}} \sim 10^{3-4} \text{ cm}^{-3}$ to $n_{\text{cr}} \sim 8 \times 10^5 \text{ cm}^{-3}$, respectively). Comparing with the thermal sound speed at 15 K, where $c_s = \sqrt{kT_K/(\mu m_{\text{H}})}$, we find an average $\sigma_{\text{NT}}/c_s = 1.6$ for NH_3 and $\sigma_{\text{NT}}/c_s = 1.1$

for N_2D^+ 3-2 emission. This comparison shows that despite the decrease in non-thermal motions, the non-thermal motions are equal in magnitude with the sound speed, even at high density. A lower gas temperature would result in even larger magnitudes of σ_{NT} , while significantly higher temperatures are unlikely.

This decrease in non-thermal motions at higher densities has been observed in starless cores (e.g., Pon et al. 2009; Tafalla et al. 2004; Lada et al. 2003). Frequently in starless cores, however, the narrowest observed line widths are consistent with being due to nearly pure thermal motions, in contrast to the results found here. As σ_{NT} values decrease, the ability for turbulent pressure to support the core against collapse is reduced, which impacts the stability of the core against its self-gravity. The narrow σ_{NT} widths found in starless cores are often explained as the result of the dissipation of turbulent motions in the core centre (Goodman et al. 1998). If the non-thermal line widths in B2 are due to turbulent motions, the corresponding turbulent pressure ($P_{\text{NT}} = mn\sigma_{\text{NT}}^2$) is equal to or greater than the thermal pressure ($P_T = nkT$).

In Paper I, we discussed the source of wide NH_3 line widths in Oph B, and concluded that if the relatively large σ_{NT} values are caused by turbulent motions, they could not be primordial (i.e., inherited from the parent cloud). This is because the damping timescale of such motions (with no external driving force) is approximately the dynamical time (Mac Low & Klessen 2004), and the existence of protostars associated with B2 implies that B2 has likely existed, with high density gas, for at least a dynamical time.

The wide lines in Oph B2 may, however, be due to more organized motions such as infall or outflow. None of the observed molecular lines are optically thick, and we therefore do not see the self-absorbed, asymmetric line profiles frequently used to infer the infall of gas within a core. Infall signatures were observed in CS, H_2CO or HCO^+ emission towards several locations in eastern B2 by André et al. (2007), but not in central or western B2. Gurney et al. (2008) observed complicated CO (and CO isotopologues) line structures towards the B2 continuum peak, but were unable to distinguish infall conclusively. The analysis of line profiles is complicated by a substantial outflow discovered in CO emission and emanating from one of the two embedded YSOs in B2 (Kamazaki et al. 2003) which extends over $10'$ (~ 0.4 pc) in size³. Upcoming results of CO, ^{13}CO and C^{18}O 3-2 observations in Ophiuchus (White et al. 2010, in preparation) from the JCMT Gould Belt Legacy Survey (GBLS, Ward-Thompson et al. 2007) will be better able to study the infall and outflow motions in Oph B. In conjunction with these data, the process of how the outflow motions affect the dense gas may be studied. There is clear evidence, however, for protostellar influence on the N_2D^+ line widths shown in Figure 5b, as discussed in §4.2. Additionally, the blue shoulder emission seen in N_2H^+ and N_2D^+ east of E32 and E33 coincides with the eastern CO lobe of the outflow, and is further evidence for the significant impact of the outflow on the dense gas.

We also noted in §4.2 that there is an offset in v_{LSR} of ~ 0.2 km s⁻¹ between N_2H^+ 4-3 and

³JCMT Spring 2009 Newsletter, <http://jach.hawaii.edu/JCMT/publications/newsletter/>

H_2D^+ emission towards B2-MM8 and the nearby embedded protostar Elias 32, with the N_2H^+ emission redshifted relative to the H_2D^+ emission. Over the rest of Oph B2, the correlation between the v_{LSR} of the two lines is good, suggesting the offset is real and localized. Comparison with N_2D^+ emission at the same location shows that the v_{LSR} of the H_2D^+ and N_2D^+ agree well, and it is consequently the N_2H^+ emission which is offset in velocity from the rest of the core gas. N_2H^+ 4-3 has a critical density approximately an order of magnitude greater than the H_2D^+ and N_2D^+ lines discussed here. The offset in v_{LSR} may thus be probing a shift in the gas motions at extremely high densities in the core interior.

5.2. Trends in the deuterium fractionation

5.2.1. The $\text{N}_2\text{D}^+/\text{N}_2\text{H}^+$ ratio

The deuterium fractionation, R_D , can be defined as the ratio between the column densities of a deuterated molecule and its hydrogen-bearing counterpart. Here, we define $R_D = N(\text{N}_2\text{D}^+)/N(\text{N}_2\text{H}^+)$, and calculate R_D in Oph B2 from $N(\text{N}_2\text{D}^+)$ calculated in §4.4.1 and $N(\text{N}_2\text{H}^+)$ calculated in Paper II. Figure 7b shows R_D across B2. The distribution is similar to the N_2D^+ column density in Figure 7a. The largest values of R_D , to a maximum $R_D = 0.16$, are found towards northeast B2, while towards the smaller scale maxima, we find $R_D \sim 0.1$ or less. We estimate we are sensitive to $R_D \sim 0.01 - 0.015$ based on the rms noise in the N_2D^+ integrated intensity map ($3\sigma \sim 0.2 \text{ K km s}^{-1}$ in the off-B2 pixels), and the mean N_2H^+ column density over Oph B2, $\langle N(\text{N}_2\text{H}^+) \rangle = 5.9 \times 10^{12} \text{ cm}^{-2}$, calculated in Paper II. We find a moderate mean $R_D = 0.03$ with an rms variation of 0.01 towards B2, comparable to results in Ori B9 towards two N_2H^+ emission peaks and a protostellar source ($R_D = 0.03 - 0.04$, Miettinen et al. 2009). While Pagani et al. (2009) find substantially greater central R_D values through modelling of the starless core L183 ($R_D \sim 0.7$ at the core centre) which decrease to ~ 0.06 at $\sim 5000 \text{ AU}$, it is not clear how to compare their model of R_D as a function of core radius to our observed column density ratio. Fontani et al. (2006) found an average $R_D \sim 0.01$ towards the high mass star forming region IRAS 05345+3157, which at high resolution resolved into two N_2D^+ condensations each with $R_D = 0.11$ (Fontani et al. 2008). In a study of starless cores, Crapsi et al. (2005) find a range in R_D between a lower limit of 0.02 to a maximum of 0.44 (which was found towards the Oph D Core). Crapsi et al. also note that R_D values > 0.1 are generally only found for cores with $N(\text{N}_2\text{H}^+) > 10^{13} \text{ cm}^{-2}$, which is approximately the maximum $N(\text{N}_2\text{H}^+)$ in Oph B2. A similar range in R_D was found towards protostellar, Class 0 sources (Emprechtinger et al. 2009). On average, then, our results agree with previous results. Given our map of Oph B2, however, we can also probe the variation of R_D across the core.

In Figure 12, we show R_D as a function of increasing $N(\text{H}_2)$ (Figure 12a), and also as a function of increasing distance (in projection) from the nearest embedded protostar (Figure 12b). Each data point represents an $18''$ pixel (to match the beam FWHM) and pixels with $\text{S/N} < 5$ in either N_2H^+ or N_2D^+ emission are omitted. No clear trend is present in the deuterium fractionation with $N(\text{H}_2)$.

We find, however, that R_D increases at greater projected distances from the embedded sources, as might be expected from the N_2D^+ integrated intensity distribution. We fit a linear trend to the data, where $R_D = (-0.007 \pm 0.002) + (0.37 \pm 0.06)d[\text{pc}]$, but note that there is large scatter in the relation. An analysis of the individual N_2H^+ and N_2D^+ abundances shows that the increasing R_D trend with projected protostellar distance is dominated by a similar increase in $X(N_2D^+)$ with projected protostellar distance, while $X(N_2H^+)$ is approximately constant over the range plotted, shown in Figure 12d.

5.2.2. H_2D^+

We next look at the distribution of the ortho- H_2D^+ abundance over Oph B2. In Figure 12, we show $X(\text{ortho-}H_2D^+)$ as a function of $N(H_2)$ (Figure 12e), and also as a function of increasing projected protostellar distance (Figure 12f). We show data in $15''$ pixels, and omit pixels with $S/N < 5$. We find no trend in the fractional ortho- H_2D^+ abundance with H_2 column density (an increasing trend is found, but not shown, in the ortho- H_2D^+ column density, $N(\text{ortho-}H_2D^+)$, with $N(H_2)$). The $X(\text{ortho-}H_2D^+)$ vs. $N(H_2)$ relationship is not entirely a scatter plot, as the ortho- H_2D^+ abundance tends to increase with projected protostellar distance to a maximum $X(\text{ortho-}H_2D^+) = 4.9 \times 10^{-10}$ at $d = 0.035$ pc, with $X(\text{ortho-}H_2D^+) \sim 1.8 \times 10^{-10}$ at larger distances. All data points at $d > 0.035$ pc correspond to the emission found in northeast B2, while the rest show emission closer to the central continuum emission peak. If we fit a linear relationship to the data, omitting the northeast B2 points, we find $X(\text{ortho-}H_2D^+) \times 10^{-10} = (1.2 \pm 0.5) + (79 \pm 23)d[\text{pc}]$.

There is also no clear trend in $N(\text{ortho-}H_2D^+)$ with R_D where both H_2D^+ and N_2D^+ are strongly detected across Oph B2, although both species are found with relatively large column densities north and west of the continuum peak. Given the small-scale structure found in the $N(N_2D^+)$ distribution in B2, the spatial resolution and sampling of our H_2D^+ observations may not be high enough to discern a correlation. We note, however, that Caselli et al. (2008) also found no clear correlation between R_D and $N(\text{ortho-}H_2D^+)$ in their sample of starless and protostellar cores (with the caveat that some R_D values were derived using column density ratios of deuterated NH_3 and deuterated H_2CO with their undeuterated counterparts rather than $N(N_2D^+)/N(N_2H^+)$). In particular, high values of R_D and relatively low $N(\text{ortho-}H_2D^+)$ were found towards two objects in Ophiuchus (Oph D and 16293E).

5.3. What is affecting the deuterium fractionation in Oph B2?

The largest deuterium fractionation values in Oph B2 are not found towards the continuum emission peak, but instead avoid the continuum peak and nearby protostars. The results of the previous section indicate that the distance to the nearest protostar is the dominant parameter impacting the deuterium fractionation in Oph B2. We next discuss several mechanisms by which the

embedded sources are most likely to impact the deuterium fractionation distribution in B2, including temperature variation in the gas, liberation of CO from dust grains, the impact of protostellar outflows, and possible increase in the ionization fraction due to x-rays from the protostars.

5.3.1. Temperature and CO depletion

Temperature can have a substantial impact on the deuterium fractionation in a dense core. As stated in §4.4.1, we expect the gas and dust to be well-coupled at the densities of Oph B2 such that $T_d = T_{gas}$, but specify in the following which of the gas or dust temperature is important in the following mechanisms. First, at $T_{gas} \gtrsim 20$ K, the H_2D^+ reaction in Equation 1 can proceed both forwards and backwards, resulting in no net increase in H_2D^+ , and consequently other deuterated species formed via reactions with H_2D^+ . Second, the CO which was deposited (adsorbed) as an icy mantle onto dust grains while at low temperatures will evaporate (desorb) back into the gas phase if the dust grains are heated, providing a destruction mechanism for H_2D^+ and again interrupting the deuteration chain.

The CO depletion factor, $f_D(\text{CO})$, is defined as the canonical CO abundance, $X_{can}(\text{CO})$, divided by the CO abundance, $X(\text{CO}) = N(\text{CO})/N(\text{H}_2)$, in the observed region:

$$f_D(\text{CO}) = \frac{X_{can}(\text{CO})}{X(\text{CO})} \quad (8)$$

such that f_D values are low where observed CO abundances are high. Low CO depletion factors can dramatically lower the H_2D^+ abundance at gas temperatures $T < 15$ K (Caselli et al. 2008). Currently no estimates of f_D exist in B2 due to a lack of data at spatial resolutions matching the available continuum data. The CO observations of the JCMT GBLS should enable the first calculations of f_D at complementary spatial resolution, and allow further analysis of the relationship between CO and the deuterium distribution in B2. The extended distribution of H_2D^+ and N_2D^+ across Oph B2 implies, however, that extensive depletion of CO has occurred. At densities of $n = 10^6 \text{ cm}^{-3}$, CO adsorption and desorption occur equally frequently when $T_d = 18$ K (Visser et al. 2009). At $T_d > 18$ K, CO will thus again become significantly more abundant in the gas phase, while at $T_{gas} > 20$ K, enhanced deuterium fractionation via Equation 1 will cease to operate.

An obvious potential source of heating is the presence of embedded protostars within Oph B2. In a 1D dynamic/chemical model of an isolated dense core which collapses to form a protostar, Aikawa et al. (2008, see their Figure 2) find temperatures greater than 18 K can be found at radii ~ 5000 AU (~ 0.02 pc) from the protostar at $\sim 10^5$ yr after its formation. As a function of total luminosity of the core, L_{core} , however, their model predicts a CO sublimation radius of $\lesssim 1000$ AU (0.005 pc) for $L_{core} \sim 0.5 - 1 L_\odot$. In a more specific example, Stamatellos et al. (2007) model the heating effect of an embedded Class I protostar ($L_{bol} = 10 L_\odot$) on the surrounding gas in the Oph A Core, and find only a small temperature increase ($\lesssim 5$ K), limited to the immediate vicinity of

the protostar, in agreement with Aikawa et al. (2008).

Both YSOs in central B2 have been classified as embedded (Jørgensen et al. 2008), Class I sources (Enoch et al. 2007). The estimated bolometric luminosities, $L_{bol} \sim 0.5 L_{\odot}$ and $\sim 1 L_{\odot}$ for E32 and E33, respectively (Enoch et al. 2007; van Kempen et al. 2009), are much smaller than used in the heating model by Stamatellos et al. (2007). The bolometric temperatures, $T_{bol} \sim 300$ K and ~ 500 K, suggest both are in the later stages of the Class I phase, as do their negative infrared spectral indices ($\alpha_{IR} = -0.03$ and -0.12). Sources with $-0.3 < \alpha_{IR} < 0$ are sometimes classified as ‘flat-spectrum’ sources, and are thought to be an intermediate stage between Class I and Class II. Crapsi et al. (2008) suggest that most or all flat-spectrum sources could be Class II objects seen edge-on. Based on these results, E32 and E33 are not likely to be deeply embedded within Oph B, and have ages $\sim 5 \times 10^5$ yr or greater based on lifetime estimates of the different protostellar stages (Evans et al. 2009).

The low luminosities of E32 and E33 suggest that they should not have a large impact on the temperature of B2, in agreement with our temperature results in Paper I which showed very little variation in the gas temperature over Oph B. Figure 12 shows that we find no trend in the kinetic temperature T_K , determined using NH_3 inversion transitions in Paper I, with protostellar distance above the $\sim 1 - 2$ K uncertainties in the data. The derived temperatures are near the required values, however, and the NH_3 temperatures may not be indicative of the conditions of the denser gas where we expect most of the deuterated species to exist. Depletion of H_2D^+ and N_2D^+ via CO sublimation would thus require an increasing temperature gradient towards higher densities near the protostars, which is not unreasonable.

Since CO also destroys N_2H^+ , significant evaporation of CO from dust grains should also be observable in the N_2H^+ distribution. Accordingly, in Figure 1b we see a decrease in the integrated N_2H^+ 1-0 intensity towards E33. No good fit to the N_2H^+ spectra was found at this location, however, due to complicated line structures, such that we are not able to determine the N_2H^+ column density or abundance. Figure 12d shows no trend on larger scales of $X(\text{N}_2\text{H}^+)$ with protostellar proximity. The N_2H^+ 4-3 distribution shows N_2H^+ remains in the gas towards E33, but an analysis of the excitation of the line would be needed to determine the N_2H^+ column density from these data.

In summary, heating by an embedded protostar can produce slightly greater gas temperatures and evaporate CO from the surface of dust grains, which would decrease the deuterium fractionation in the gas. Since we do not see evidence of a decrease in $X(\text{N}_2\text{H}^+)$ towards the protostars, the evaporation of CO from dust grains is likely not the major mechanism for the decrease in abundance of deuterated species. While we also don’t see evidence of increased gas temperatures near the protostars in the NH_3 data, these temperatures reflect average values along the line-of-sight, and do not rule out increased temperatures at higher densities near the protostars. Given the strong dependence of increased deuterium fractionation on temperature, we expect this mechanism is likely very important in B2.

5.3.2. *The Oph B2 outflow*

The deuterium fractionation may be impacted by the known, extensive CO outflow in B2 described in §5.1. It appears that the dense gas in eastern Oph B2 is affected by the outflow, given the larger line widths seen towards the protostars in high density tracers, changes in v_{LSR} , and the blue shoulder emission which is coincident with the eastern lobe of the outflow (Kamazaki et al. 2003) (although large line widths could also indicate the presence of infall motions). We do not find evidence of outflow interaction with the dense gas in northwest Oph B2, suggesting that the outflow may be in front of or behind the bulk of the core gas. Very localized heating of the surrounding gas by the protostar could evaporate CO from the dust grains. The outflow, then containing entrained CO, could mix the CO with the dense core gas, destroying the deuterated species without an increase in the gas temperature on larger scales. Alternatively, shocks associated with the outflow could raise gas temperatures and reintroduce enough CO to the gas phase to affect the deuterium fractionation. Further analysis of the outflow, including observations of shock tracers, is needed to determine whether this scenario is reasonable, and can examine the impact of low-mass protostellar outflows on dense gas chemistry. As discussed above, however, we do not find evidence for variation in the N_2H^+ abundance as would be expected if destruction due to gas-phase CO is the dominant mechanism for decreasing the abundance of deuterated species relative to their non-deuterated counterparts.

5.3.3. *Ionization fraction and electron abundance x_e*

Variations in the ionization fraction in the dense gas can also affect the deuterium fractionation, in particular in regions of high CO depletion. The electron abundance, $x_e = n_e/n_{H_2}$, is the ratio of the electron number density (n_e) with the number density of molecular hydrogen, n_{H_2} , and is equivalent to the ionization fraction. The deuterium fraction can be reduced by an increase in x_e , which in turn increases the rate of dissociative recombination (Caselli et al. 2008). The abundances of deuterated molecules can thus be used as a probe of x_e in dense cores. At high extinction towards starless cores, the creation of ions is expected to be dominated by the cosmic ray flux, with $x_e \propto n_{H_2}^{-1/2}$ (McKee 1989).

Studies investigating x_e in dense cores using the DCO^+/HCO^+ ratio have found average line-of-sight $x_e \sim 10^{-7}$ (Bergin & Tafalla 2007, and references therein). In regions of high depletion, the column density ratio of N_2D^+ with N_2H^+ is expected to be a better probe of x_e than the ratio of DCO^+ with HCO^+ . Since H_3^+ is expected to be the major molecular ion in cores strongly depleted in heavy elements, we can use observations of H_2D^+ , in conjunction with R_D , to set limits on x_e assuming the numbers of positive and negative charges are approximately equal (i.e., the core gas is neutral). Given the abundances of N_2H^+ , N_2D^+ and H_2D^+ in B2, we can thus derive a lower limit on x_e following Miettinen et al. (2009):

$$x_e > X(\text{N}_2\text{H}^+) + X(\text{N}_2\text{D}^+) + X(\text{H}_3^+) + X(\text{H}_2\text{D}^+) \quad (9)$$

where we neglect multiply deuterated forms of H_3^+ . As discussed in §4.4.2, predictions of the o/p- H_2D^+ ratio vary from ~ 0.1 to $\gtrsim 1$, and we use a moderate o/p- $\text{H}_2\text{D}^+ = 0.5$ to estimate $X(\text{H}_2\text{D}^+)$ from $X(\text{ortho-}\text{H}_2\text{D}^+)$. In a simple, steady state analytical model, Crapsi et al. (2004) relate R_D (where $R_D = N(\text{N}_2\text{D}^+) / N(\text{N}_2\text{H}^+)$) to the relative H_2D^+ - H_3^+ abundance, $r = [\text{H}_2\text{D}^+] / [\text{H}_3^+]$, and also neglect multiply deuterated forms of H_3^+ such that $R_D \approx r / (3 + 2r)$. In an updated result, Miettinen et al. (2009) find $R_D \approx (r + 2r^2) / (3 + 2r + r^2)$. Using the Miettinen et al. relation we then find a mean $r = 0.07$ across Oph B2, and a lower limit $x_e > 1.5 \times 10^{-8}$ through Equation 9. We find small variations in the lower limit across B2, with a larger limit $x_e > 2.7 \times 10^{-8}$ towards Elias 32 and higher values in general near the $850 \mu\text{m}$ continuum peak. Detailed modeling, in conjunction with a measurement of the CO depletion factor in B2, is needed to improve this analysis of x_e beyond a lower limit only.

Low mass protostars emit x-rays, which could potentially increase the local ionization fraction and consequently decrease locally the deuterium fractionation of gas in Oph B2. In their study of the x-ray emission from young protostars in the central Ophiuchus region with ROSAT, Casanova et al. (1995) detected both Oph B2 protostars in the 1 – 2.4 keV range, finding luminosities (adjusted for extinction) $L_x = 30.7 \text{ erg s}^{-1}$ and $L_x = 29.2 \text{ erg s}^{-1}$ for E32 and E33, respectively. We can then estimate the x-ray ionization rate due to the protostars, ζ_x , at a distance r following Silk & Norman (1983, Equation 2). From Figure 12, we find trends in R_D and $X(\text{ortho-}\text{H}_2\text{D}^+)$ to projected protostellar distances of order a few $\times 0.01$ pc. Assuming a constant, uniform density $n = 10^5 \text{ cm}^{-3}$, at $r = 0.02 \text{ pc}$ we find $\zeta_x \sim 9 \times 10^{-17} \text{ s}^{-1}$, and at $r = 0.04 \text{ pc}$ we find $\zeta_x \sim 8 \times 10^{-18} \text{ s}^{-1}$. The fractional ionization based on these rates, again following Silk & Norman, is $x_e \sim 9 \times 10^{-8}$ and $x_e \sim 3 \times 10^{-8}$ at $r = 0.02 \text{ pc}$ and $r = 0.04 \text{ pc}$, consistent with our lower limits calculated above. Clumpy, rather than uniform gas could allow x-rays to penetrate further into the core, potentially increasing the fractional ionization to greater distances. The standard ionization rate due to cosmic rays alone $\zeta_{CR} = 1.3 \times 10^{-17} \text{ s}^{-1}$ (Herbst & Klemperer 1973), leading to a fractional ionization $x_e \sim 4 \times 10^{-8}$ for $n = 10^5 \text{ cm}^{-3}$ (McKee 1989). Our simple calculation shows that at distances comparable to where we find variation in the deuterium fractionation in Oph B2, the protostellar x-ray ionization rate and resulting fractional ionization may be comparable to or greater than expected due to cosmic rays alone. This result suggests that x-ray ionization is a viable mechanism to depress the deuterium fractionation close to embedded protostars. Further work is needed to directly measure the fractional ionization of dense gas near protostars, and to quantify the effect of a greater ionization rate on the chemical network of deuterated species in high density gas.

5.3.4. Other possibilities

While Figure 12 suggests that the distribution of enhanced deuterium fractionation of H_3^+ and

N_2H^+ in Oph B2 is tied to the presence of the Class I protostars associated with the core, other factors may influence the deuteration chemistry in this complex environment. For completeness, we briefly mention two other possibilities. First, line-of-sight inhomogeneities in Oph B2 would impact our estimate of the deuterium fractionation, as our analysis assumes constant excitation and abundance conditions along the line of sight. Detailed physical and chemical modeling may be useful in probing the effects of possible inhomogeneities, but is beyond the scope of this paper due to the complexity of Oph B2. Second, differences in the evolutionary timescale may be important in Oph B2, and in other multiple-star-forming objects. While several protostars have already formed out of the core gas (particularly in the south), there remain multiple dense, starless clumps within B2 which may yet form stars. The timescale on which different parts of the core condense and collapse may impact the dense gas chemistry and produce variations in the deuterium fractionation across Oph B2.

In summary, there are a number of different mechanisms by which the deuterium fractionation of N_2H^+ and H_3^+ may be decreased near young protostars. We feel that a local increase in the gas temperature is the most likely explanation of this trend, but our simple calculation of the expected increase in the ionization fraction above the standard cosmic ray value is intriguing and worth further study.

6. Summary

In this paper we have presented the results of N_2D^+ 3-2, N_2H^+ 4-3 and ortho- H_2D^+ $1_{11} - 1_{10}$ mapping of the cluster-forming Ophiuchus B Core. In general, our results show that care must be taken when using deuterated species as a probe of the physical conditions of dense gas conditions in star-forming regions. We summarize in detail our results below.

1. Significant emission from the deuterated species N_2D^+ and H_2D^+ extends over several square arcminutes in B2. In particular, the extent of the H_2D^+ emission is the largest yet mapped. Both species' integrated intensity distributions are offset from the continuum emission, and avoid entirely parts of B2 near embedded protostars and the peak of continuum emission from cold dust.

2. Through fitting of the spectral lines, we find greater N_2D^+ line widths near protostars embedded in B2, suggestive of protostellar influence on the dense gas. Complicated line structures are found, including blue line shoulders, in all three tracers. We estimate the non-thermal line widths for the species observed here and compare with NH_3 and N_2H^+ results from Paper I and Paper II. In B2, non-thermal line widths decrease with increasing critical density of the molecular tracer, but remain transonic or only slightly subsonic even at high densities. This result is in contrast with the nearly thermal line widths found in many isolated cores.

3. We test a method to estimate the gas temperature by equating the non-thermal line widths of N_2D^+ and H_2D^+ and solving for T_K . We find both realistic ($T_K \sim 11$ K) and unrealistic ($T_K < 0$ K and $T_K \gtrsim 25$ K) values in B2. Complicated line structure in B2 likely affects this analysis, but we expect good results can be found in regions with simple velocity structure.

4. The deuterium fraction of N_2H^+ $R_D = N(N_2D^+)/N(N_2H^+) \sim 0.03$ on average where N_2D^+ is detected. Small-scale features of enhanced R_D are seen in B2, but most do not correlate with previously identified continuum clumps or N_2H^+ clumps. This R_D is consistent with previous results in protostellar cores, and is also within the lower range of values found for starless cores.

5. The average ortho- H_2D^+ abundance, $X(\text{ortho-}H_2D^+) \sim 3 \times 10^{-10}$, given an assumed excitation temperature of 12 K. An accurate measure of the ortho- to para- H_2D^+ ratio is needed to convert to total H_2D^+ abundance, and has been found in previous studies to vary between 0.1 and > 1 . Future observations of para- H_2D^+ transitions, if possible, are needed to constrain this value in dense cores.

6. An anti-correlation is found with R_D and $X(\text{ortho-}H_2D^+)$ and projected distance to the nearest embedded protostar in B2. This relation indicates that the embedded protostars in B2 are affecting the internal chemistry. Possible mechanisms are through gas heating, evaporation of CO off dust grains, CO mixing caused by the B2 outflow, or by increasing the local ionization fraction. Gas temperatures determined through NH_3 analysis in Paper I are $< 18\text{--}20$ K required to evaporate CO and reduce deuterium fractionation, but NH_3 may not be a good tracer of conditions in the high density gas in Oph B2. We calculate that the x-ray flux of the embedded protostars in B2 could increase the fractional ionization of the core gas beyond that expected solely due to cosmic ray ionization to distances $\sim 0.02 - 0.03$ pc, similar to the distances over which we find variation in the deuterium fractionation. We suggest that a temperature increase is the dominant parameter in this trend, but further research on the effect of young stars and their outflows on both the local ionization fraction and the chemistry of deuterated species in protostellar cores is needed.

7. We use the observed R_D and $X(\text{ortho-}H_2D^+)$ to estimate a lower limit on the ionization fraction in B2, and find $x(e) > 1.5 \times 10^{-8}$ given an assumed ortho- to para- H_2D^+ ratio of 0.5.

We thank the anonymous referee and E. Feigelson for comments which improved the paper. We also thank H. Kirk for providing SCUBA maps of the regions observed and H. Weisemeyer for help with the IRAM observations. The National Radio Astronomy Observatory is a facility of the National Science Foundation operated under cooperative agreement by Associated Universities, Inc. The James Clerk Maxwell Telescope is operated by the Joint Astronomy Centre on behalf of the Particle Physics and Astronomy Research Council of the United Kingdom, the Netherlands Association for Scientific Research, and the National Research Council of Canada. RKF acknowledges financial support from the University of Victoria and the National Research Council Canada Graduate Student Scholarship Supplement Program. We also acknowledge the support of the National Science and Engineering Research Council of Canada. This research is supported in part by the National Science Foundation under grant number 0708158 (TLB).

Facilities: JCMT, IRAM

REFERENCES

- Aikawa, Y., Wakelam, V., Garrod, R. T., & Herbst, E. 2008, *ApJ*, 674, 984
- Amano, T. & Hirao, T. 2005, *Journal of Molecular Spectroscopy*, 233, 7
- André, P., Belloche, A., Motte, F., & Peretto, N. 2007, *A&A*, 472, 519
- Bergin, E. A. & Tafalla, M. 2007, *ARA&A*, 45, 339
- Buckle, J. V., Hills, R. E., Smith, H., Dent, W. R. F., Bell, G., Curtis, E. I., Dace, R., Gibson, H., Graves, S. F., Leech, J., Richer, J. S., Williamson, R., Withington, S., Yassin, G., Bennett, R., Hastings, P., Laidlaw, I., Lightfoot, J. F., Burgess, T., Dewdney, P. E., Hovey, G., Willis, A. G., Redman, R., Wooff, B., Berry, D. S., Cavanagh, B., Davis, G. R., Dempsey, J., Friberg, P., Jenness, T., Kackley, R., Rees, N. P., Tilanus, R., Walther, C., Zwart, W., Klapwijk, T. M., Kroug, M., & Zijlstra, T. 2009, *MNRAS*, 399, 1026
- Casanova, S., Montmerle, T., Feigelson, E. D., & Andre, P. 1995, *ApJ*, 439, 752
- Caselli, P., Benson, P. J., Myers, P. C., & Tafalla, M. 2002a, *ApJ*, 572, 238
- Caselli, P., van der Tak, F. F. S., Ceccarelli, C., & Bacmann, A. 2003, *A&A*, 403, L37
- Caselli, P., Vastel, C., Ceccarelli, C., van der Tak, F. F. S., Crapsi, A., & Bacmann, A. 2008, *A&A*, 492, 703
- Caselli, P., Walmsley, C. M., Zucconi, A., Tafalla, M., Dore, L., & Myers, P. C. 2002b, *ApJ*, 565, 331
- . 2002c, *ApJ*, 565, 344
- Crapsi, A., Caselli, P., Walmsley, C. M., Myers, P. C., Tafalla, M., Lee, C. W., & Bourke, T. L. 2005, *ApJ*, 619, 379
- Crapsi, A., Caselli, P., Walmsley, C. M., Tafalla, M., Lee, C. W., Bourke, T. L., & Myers, P. C. 2004, *A&A*, 420, 957
- Crapsi, A., van Dishoeck, E. F., Hogerheijde, M. R., Pontoppidan, K. M., & Dullemond, C. P. 2008, *A&A*, 486, 245
- Daniel, F., Cernicharo, J., Roueff, E., Gerin, M., & Dubernet, M. L. 2007, *ApJ*, 667, 980
- Dore, L., Caselli, P., Beninati, S., Bourke, T., Myers, P. C., & Cazoli, G. 2004, *A&A*, 413, 1177
- Elias, J. H. 1978, *ApJ*, 224, 453
- Emprechtinger, M., Caselli, P., Volgenau, N. H., Stutzki, J., & Wiedner, M. C. 2009, *A&A*, 493, 89
- Enoch, M. L., Evans, N. J., Sargent, A. I., & Glenn, J. 2009, *ApJ*, 692, 973

- Enoch, M. L., Glenn, J., Evans, II, N. J., Sargent, A. I., Young, K. E., & Huard, T. L. 2007, *ApJ*, 666, 982
- Evans, N. J., Dunham, M. M., Jørgensen, J. K., Enoch, M. L., Merín, B., van Dishoeck, E. F., Alcalá, J. M., Myers, P. C., Stapelfeldt, K. R., Huard, T. L., Allen, L. E., Harvey, P. M., van Kempen, T., Blake, G. A., Koerner, D. W., Mundy, L. G., Padgett, D. L., & Sargent, A. I. 2009, *ApJS*, 181, 321
- Flower, D. R., Pineau Des Forêts, G., & Walmsley, C. M. 2006, *A&A*, 449, 621
- Fontani, F., Caselli, P., Bourke, T. L., Cesaroni, R., & Brand, J. 2008, *A&A*, 477, L45
- Fontani, F., Caselli, P., Crapsi, A., Cesaroni, R., Molinari, S., Testi, L., & Brand, J. 2006, *A&A*, 460, 709
- Friesen, R. K., Di Francesco, J., Shimajiri, Y., & Takakuwa, S. 2010, *ApJ*, 708, 1002
- Friesen, R. K., Di Francesco, J., Shirley, Y. L., & Myers, P. C. 2009, *ApJ*, 697, 1457
- Fuller, G. A. & Myers, P. C. 1993, *ApJ*, 418, 273
- Gerin, M., Pearson, J. C., Roueff, E., Falgarone, E., & Phillips, T. G. 2001, *ApJ*, 551, L193
- Goodman, A. A., Barranco, J. A., Wilner, D. J., & Heyer, M. H. 1998, *ApJ*, 504, 223
- Gurney, M., Plume, R., & Johnstone, D. 2008, *PASP*, 120, 1193
- Herbst, E. & Klemperer, W. 1973, *ApJ*, 185, 505
- Johnstone, D., Di Francesco, J., & Kirk, H. 2004, *ApJ*, 611, L45
- Johnstone, D., Wilson, C. D., Moriarty-Schieven, G., Joncas, G., Smith, G., Gregersen, E., & Fich, M. 2000, *ApJ*, 545, 327
- Jørgensen, J. K., Johnstone, D., Kirk, H., Myers, P. C., Allen, L. E., & Shirley, Y. L. 2008, *ApJ*, 683, 822
- Kamazaki, T., Saito, M., Hirano, N., Umemoto, T., & Kawabe, R. 2003, *ApJ*, 584, 357
- Kirk, H., Johnstone, D., & Di Francesco, J. 2006, *ApJ*, 646, 1009
- Lada, C. J., Bergin, E. A., Alves, J. F., & Huard, T. L. 2003, *ApJ*, 586, 286
- Lombardi, M., Lada, C. J., & Alves, J. 2008, *A&A*, 480, 785
- Loren, R. B., Wootten, A., & Wilking, B. A. 1990, *Astrophys. J.*, 365, 269
- Mac Low, M.-M. & Klessen, R. S. 2004, *Reviews of Modern Physics*, 76, 125

- McKee, C. F. 1989, *ApJ*, 345, 782
- Miettinen, O., Harju, J., Haikala, L. K., Kainulainen, J., & Johansson, L. E. B. 2009, ArXiv e-prints
- Millar, T. J., Bennett, A., & Herbst, E. 1989, *ApJ*, 340, 906
- Motte, F., Andre, P., & Neri, R. 1998, *A&A*, 336, 150
- Pagani, L., Daniel, F., & Dubernet, M.-L. 2009, *A&A*, 494, 719
- Pon, A., Plume, R., Friesen, R. K., Di Francesco, J., Matthews, B., & Bergin, E. A. 2009, *ApJ*, 698, 1914
- Ramanlal, J. & Tennyson, J. 2004, *MNRAS*, 354, 161
- Sadavoy, S. I., Di Francesco, J., Bontemps, S., Megeath, S. T., Rebull, L. M., Allgaier, E., Carey, S., Gutermuth, R., Hora, J., Huard, T., McCabe, C., Muzerolle, J., Noriega-Crespo, A., Padgett, D., & Terebey, S. 2010, *ApJ*, 710, 1247
- Sastry, K. V. L. N., Helminger, P., Herbst, E., & De Lucia, F. C. 1981, *Chem. Phys. Lett.*, 84, 286
- Schöier, F. L., van der Tak, F. F. S., van Dishoeck, E. F., & Black, J. H. 2005, *A&A*, 432, 369
- Schuster, K.-F., Boucher, C., Brunswig, W., Carter, M., Chenu, J.-Y., Foullieux, B., Greve, A., John, D., Lazareff, B., Navarro, S., Perrigouard, A., Pollet, J.-L., Sievers, A., Thum, C., & Wiesemeyer, H. 2004, *A&A*, 423, 1171
- Silk, J. & Norman, C. 1983, *ApJ*, 272, L49
- Sipilä, O., Hugo, E., Harju, J., Asvany, O., Juvela, M., & Schlemmer, S. 2010, *A&A*, 509, A260000+
- Smith, H., Buckle, J., Hills, R., Bell, G., Richer, J., Curtis, E., Withington, S., Leech, J., Williamson, R., Dent, W., Hastings, P., Redman, R., Wooff, B., Yeung, K., Friberg, P., Walther, C., Kackley, R., Jenness, T., Tilanus, R., Dempsey, J., Kroug, M., Zijlstra, T., & Klapwijk, T. M. 2008, in *Society of Photo-Optical Instrumentation Engineers (SPIE) Conference Series*, Vol. 7020, Society of Photo-Optical Instrumentation Engineers (SPIE) Conference Series
- Stamatellos, D., Whitworth, A. P., & Ward-Thompson, D. 2007, *MNRAS*, 379, 1390
- Stark, R., Sandell, G., Beck, S. C., Hogerheijde, M. R., van Dishoeck, E. F., van der Wal, P., van der Tak, F. F. S., Schäfer, F., Melnick, G. J., Ashby, M. L. N., & de Lange, G. 2004, *ApJ*, 608, 341
- Stark, R., van der Tak, F. F. S., & van Dishoeck, E. F. 1999, *ApJ*, 521, L67
- Tafalla, M., Myers, P. C., Caselli, P., & Walmsley, C. M. 2004, *A&A*, 416, 191

- van Kempen, T. A., van Dishoeck, E. F., Salter, D. M., Hogerheijde, M. R., Jørgensen, J. K., & Boogert, A. C. A. 2009, *A&A*, 498, 167
- Vastel, C., Caselli, P., Ceccarelli, C., Phillips, T., Wiedner, M. C., Peng, R., Houde, M., & Dominik, C. 2006, *ApJ*, 645, 1198
- Vastel, C., Phillips, T. G., & Yoshida, H. 2004, *ApJ*, 606, L127
- Visser, R., van Dishoeck, E. F., Doty, S. D., & Dullemond, C. P. 2009, *A&A*, 495, 881
- Vrba, F. J., Strom, K. M., Strom, S. E., & Grasdalen, G. L. 1975, *ApJ*, 197, 77
- Walmsley, C. M., Flower, D. R., & Pineau des Forêts, G. 2004, *A&A*, 418, 1035
- Ward-Thompson, D., Di Francesco, J., Hatchell, J., Hogerheijde, M. R., Nutter, D., Bastien, P., Basu, S., Bonnell, I., Bowey, J., Brunt, C., Buckle, J., Butner, H., Cavanagh, B., Chrysostomou, A., Curtis, E., Davis, C. J., Dent, W. R. F., van Dishoeck, E., Edmunds, M. G., Fich, M., Fiege, J., Fissel, L., Friberg, P., Friesen, R., Frieswijk, W., Fuller, G. A., Gosling, A., Graves, S., Greaves, J. S., Helmich, F., Hills, R. E., Holland, W. S., Houde, M., Jayawardhana, R., Johnstone, D., Joncas, G., Kirk, H., Kirk, J. M., Knee, L. B. G., Matthews, B., Matthews, H., Matzner, C., Moriarty-Schieven, G. H., Naylor, D., Padman, R., Plume, R., Rawlings, J. M. C., Redman, R. O., Reid, M., Richer, J. S., Shipman, R., Simpson, R. J., Spaans, M., Stamatellos, D., Tsamis, Y. G., Viti, S., Weferling, B., White, G. J., Whitworth, A. P., Wouterloot, J., Yates, J., & Zhu, M. 2007, *PASP*, 119, 855
- Williams, J. P., de Geus, E. J., & Blitz, L. 1994, *ApJ*, 428, 693
- Young, K. E., Enoch, M. L., Evans, II, N. J., Glenn, J., Sargent, A., Huard, T. L., Aguirre, J., Golwala, S., Haig, D., Harvey, P., Laurent, G., Maukopf, P., & Sayers, J. 2006, *ApJ*, 644, 326

Table 1. Observed Species, Transitions and Rest Frequencies

Species	Transition	F'_1	F'	F_1	F	Frequency GHz
N_2D^+	3 – 2	4	5	3	4	231.321906 ^a
N_2H^+	4 – 3	5	5	4	4	372.672494 ^b
H_2D^+	1 ₁₁ – 1 ₁₀					372.421385 ^c

^aGerin et al. (2001)

^bPagani et al. (2009)

^cAmano & Hirao (2005)

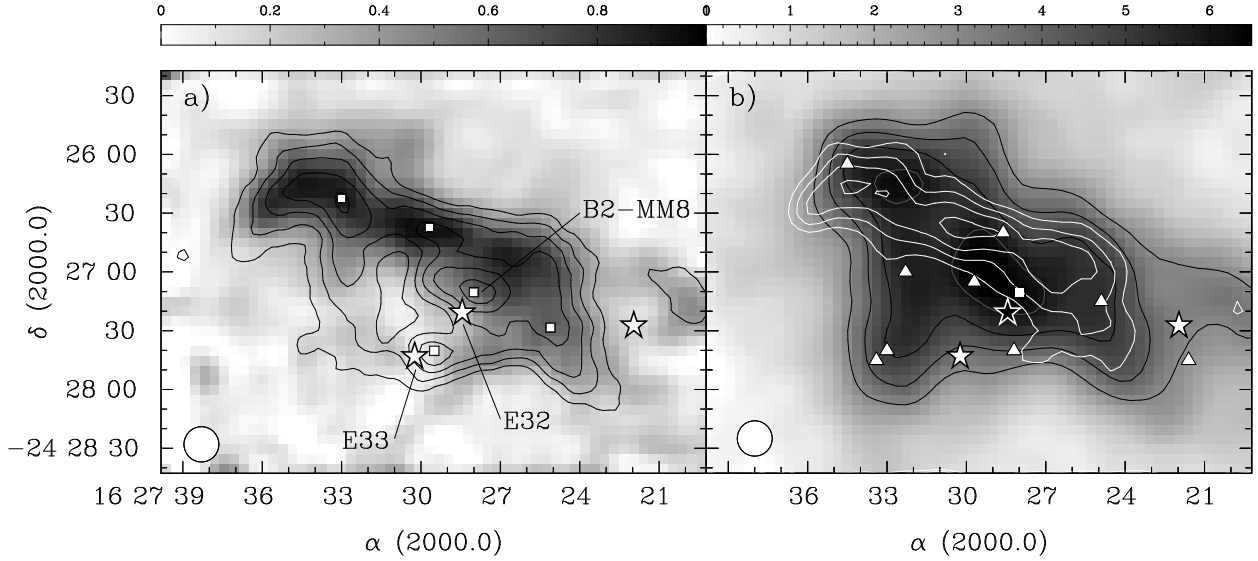


Fig. 1.— a) Integrated N_2D^+ 3-2 emission towards Oph B2 (greyscale) in T_B units. Data have been convolved to a final $18''$ beam (FWHM). Black contours show $850\ \mu\text{m}$ continuum emission in increments of $0.1\ \text{Jy beam}^{-1}$. Squares show the locations of continuum clumps identified by Jørgensen et al. (2008). The continuum clump B2-MM8 is identified. In both plots, stars indicate the positions of Class I protostars (with Elias 32 and 33 identified) and the $18''$ beam is shown at lower left. b) Integrated N_2H^+ 1-0 emission towards Oph B2 observed with the Nobeyama 45 m Telescope at $18''$ (FWHM) resolution (greyscale). Black and grey contours begin at $3\ \text{K km s}^{-1}$ (T_{MB}) and increase by $1\ \text{K km s}^{-1}$. Triangles show the peak locations of N_2H^+ clumps identified with CLUMPFIND, and the continuum clump B2-MM8 is shown by the square. White contours trace N_2D^+ emission from a), beginning at $0.45\ \text{K km s}^{-1}$ (T_B) and increasing by $0.15\ \text{K km s}^{-1}$.

Table 2. Mean NH_3 , N_2H^+ , N_2D^+ and H_2D^+ v_{LSR} and Δv in Oph B2

Species	Transition	v_{LSR} km s^{-1}				Δv km s^{-1}				n_{cr} cm^{-3}
		Mean	RMS	Min	Max	Mean	RMS	Min	Max	
NH_3	$(J, K) = (1, 1)$	4.14	0.19	3.85	4.58	0.87	0.16	0.42	1.11	2×10^4 ^a
N_2H^+	$J = 1 - 0$	4.04	0.20	3.61	4.43	0.71	0.22	0.38	1.42	1.4×10^5 ^b
H_2D^+	J_{K-1K_1} $= 1_{11} - 1_{10}$	4.01	0.24	3.65	4.50	0.74	0.19	0.51	1.36	$\sim 10^5$ ^c
N_2D^+	$J = 3 - 2$	4.02	0.19	3.67	4.44	0.53	0.20	0.25	1.36	8×10^5 ^d
N_2H^+	$J = 4 - 3$ ^e	4.05	0.22	3.39	4.43	0.69	0.18	0.47	1.14	7.7×10^6 ^b

Note. — The velocity resolution of the NH_3 observations was 0.3 km s^{-1} . All other species were observed with 0.1 km s^{-1} velocity resolution or better.

^aCaselli et al. (2002a)

^bSchöier et al. (n_{cr} calculated using Einstein A coefficients and collision rates γ_{ul} at 10 K from the Leiden Atomic and Molecular Database; 2005)

^cCaselli et al. (2008)

^dCalculated using Einstein A coefficients and collision rates for N_2H^+ 3-2 at 10 K (Schöier et al. 2005). Daniel et al. (2007) (see their Figure 17) found that despite small differences in Einstein A coefficients and collision rates, critical densities of N_2H^+ and N_2D^+ are similar for transitions other than $J = 1 - 0$.

^eValues calculated from a Gaussian fit due to a lack of visible hyperfine structure. The reported line widths may be greater by $\sim 10 - 25\%$ than the true values; see §4.1.

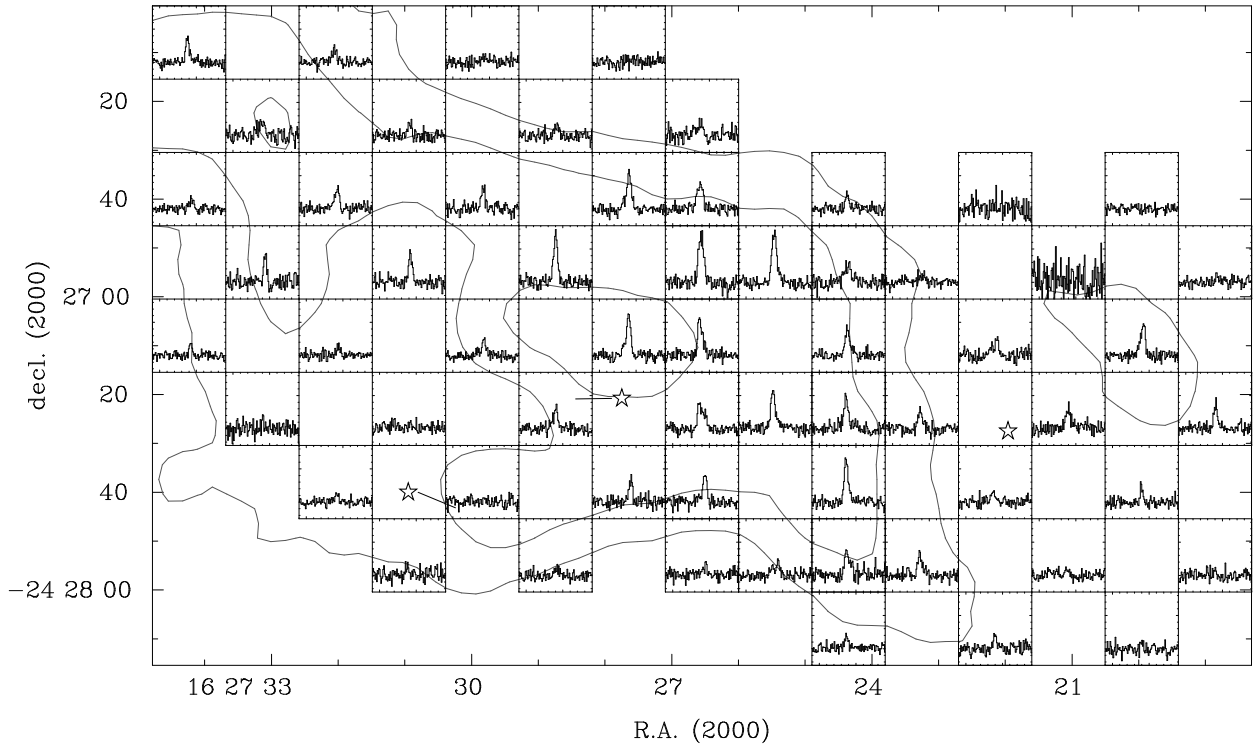


Fig. 2.— H_2D^+ $1_{11} - 1_{10}$ spectra observed with HARP at the JCMT towards Oph B2 with $15''$ FWHM. The grey contours show $850\ \mu\text{m}$ continuum emission observed at the same resolution at $0.1\ \text{Jy beam}^{-1}$, $0.3\ \text{Jy beam}^{-1}$ and $0.5\ \text{Jy beam}^{-1}$. Stars represent Class I protostars, with solid lines indicating the location if within a spectrum box. The velocity scale on the subplots runs from $-1\ \text{km s}^{-1}$ to $9\ \text{km s}^{-1}$, while the amplitude ranges from $-0.25\ \text{K}$ to $0.85\ \text{K}$ (T_{MB} , assuming $\eta_{MB} = 0.6$).

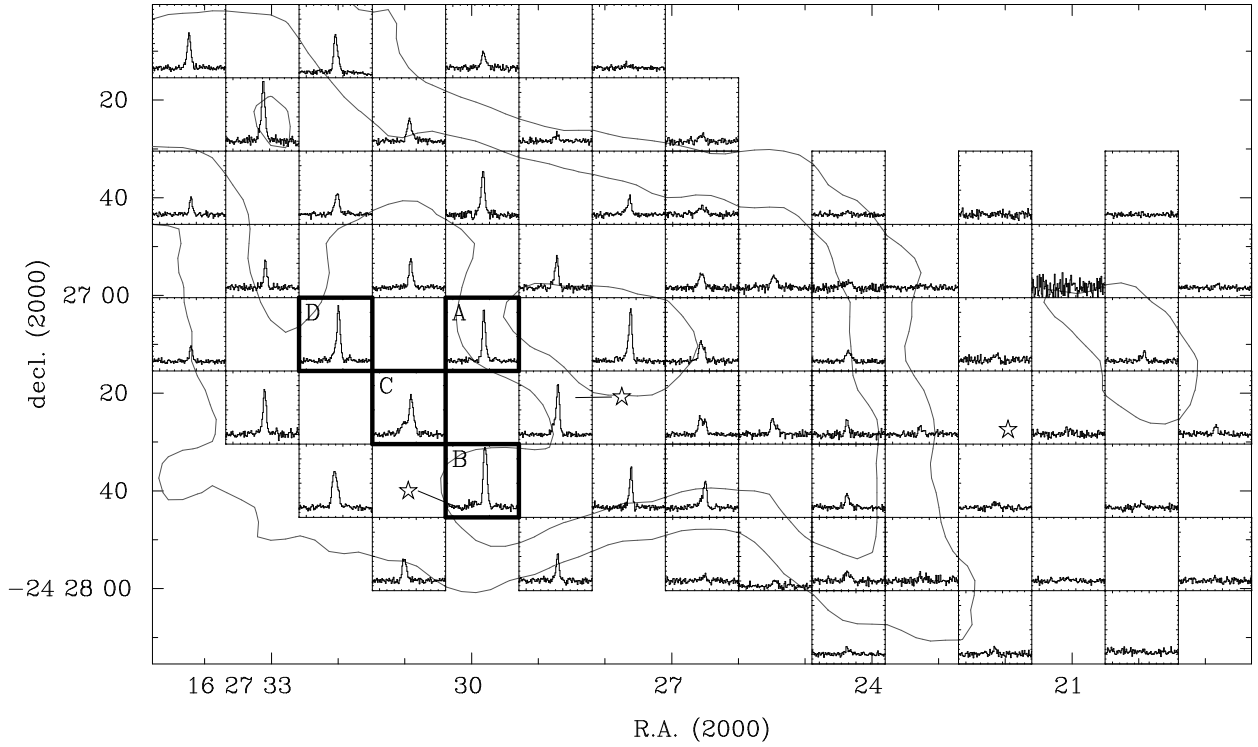


Fig. 3.— N_2H^+ 4-3 spectra observed with HARP at the JCMT towards Oph B2 with $15''$ FWHM. The grey contours, stars and velocity scale on the subplots are as in Figure 2. The amplitude ranges from -0.3 K to 2.2 K (T_{MB} , assuming $\eta_{MB} = 0.6$). Four locations of interesting spectra, labeled A, B, C and D, are highlighted by dark outlines.

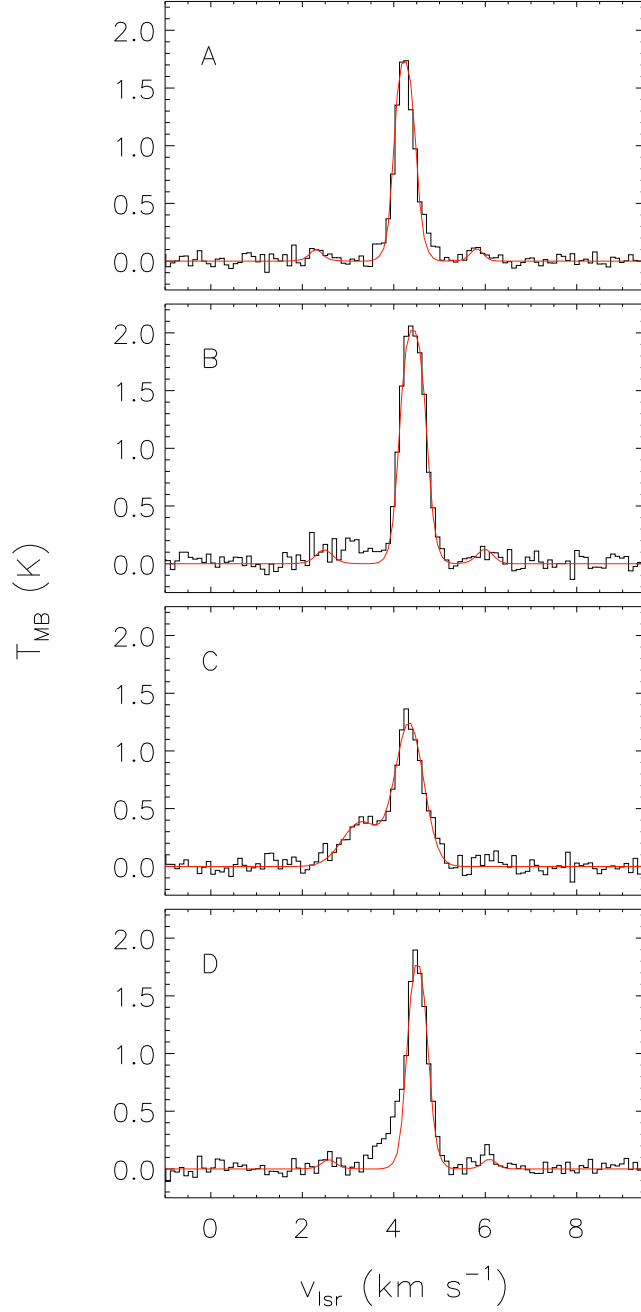


Fig. 4.— N_2H^+ 4-3 spectra towards four locations in Oph B2, labeled A, B, C and D in Figure 3: 30'' north of E33 (A), towards E33 (B), 21'' north-east of E33 (C), and $\sim 42''$ north-east of E33 (D). Overlaid on the spectra are fits to the full hyperfine structure of the N_2H^+ 4-3 line (A, B and D) and a two-component Gaussian fit (C).

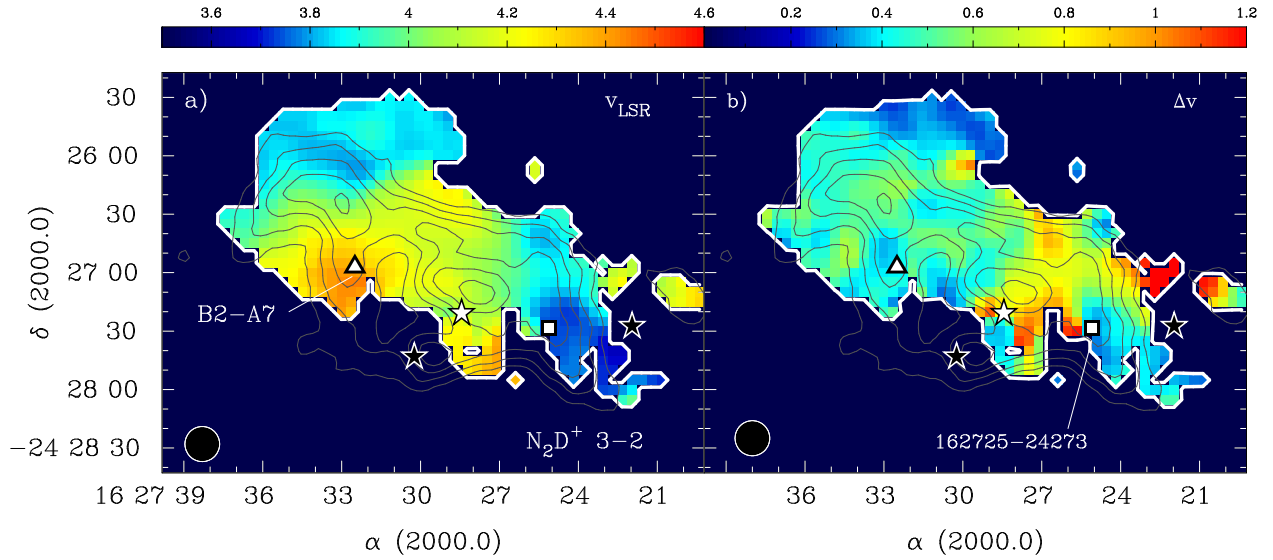


Fig. 5.— a) N_2D^+ 3-2 line velocity or v_{LSR} in Oph B2. Colour scale is in km s^{-1} . In both plots, only results from pixels where the S/N of the peak line intensity is ≥ 5 are shown, indicated by the solid white contour. Contours show $850 \mu\text{m}$ continuum emission at $15''$ (FWHM) resolution observed with the JCMT, in increments of 0.1 Jy beam^{-1} . The $18''$ (FWHM) beam is shown at lower left. Stars indicate the positions of Class I protostars. The locations of the NH_3 clump B2-A7 and $850 \mu\text{m}$ continuum clump 16275-2422 are also shown. b) Fitted Δv in Oph B2, contours as in a). Colour scale is in km s^{-1} .

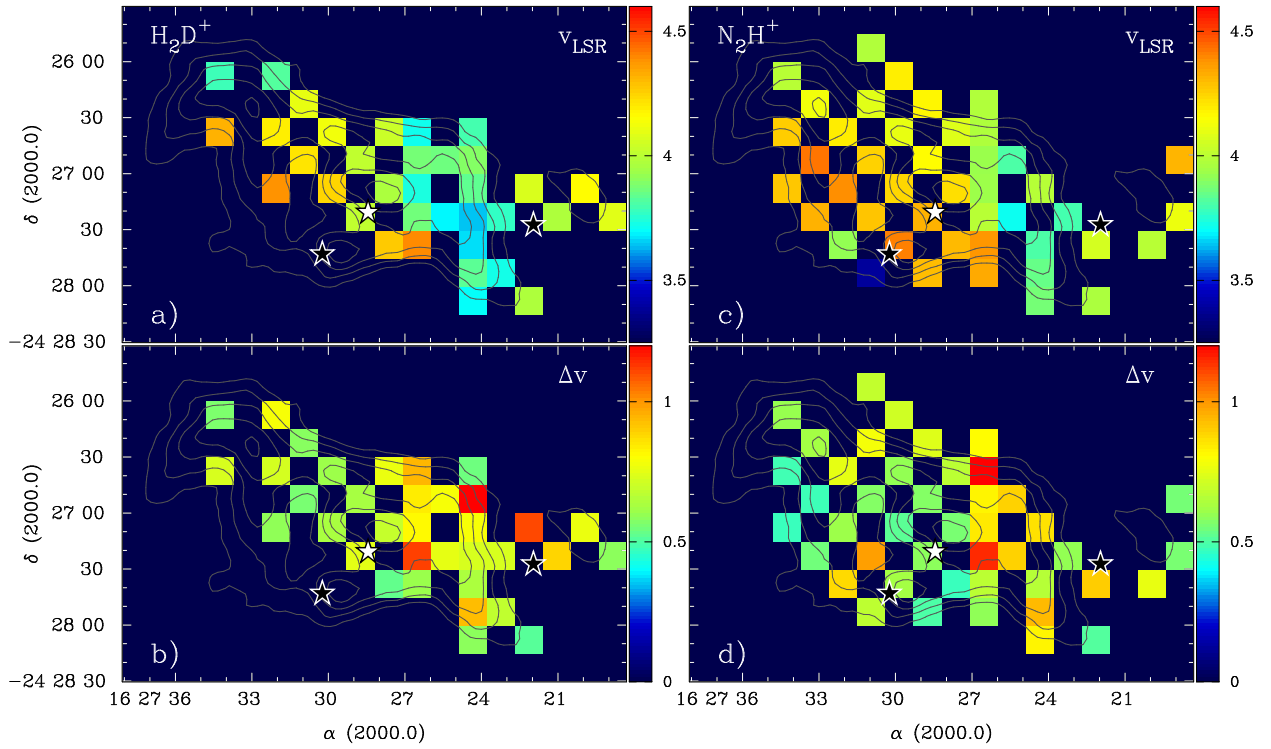


Fig. 6.— a, c) H_2D^+ $1_{11} - 1_{10}$ and N_2H^+ $4-3$ line velocity v_{LSR} in Oph B2, respectively. Colour scale is in km s^{-1} . We show only results from pixels where the S/N of the peak line intensity is ≥ 5 . Grey contours show $850 \mu\text{m}$ continuum emission as in Figure 5. Stars indicate positions of embedded Class I protostars. b, d) H_2D^+ and N_2H^+ line width Δv in Oph B2, respectively. Colour scale is in km s^{-1} .

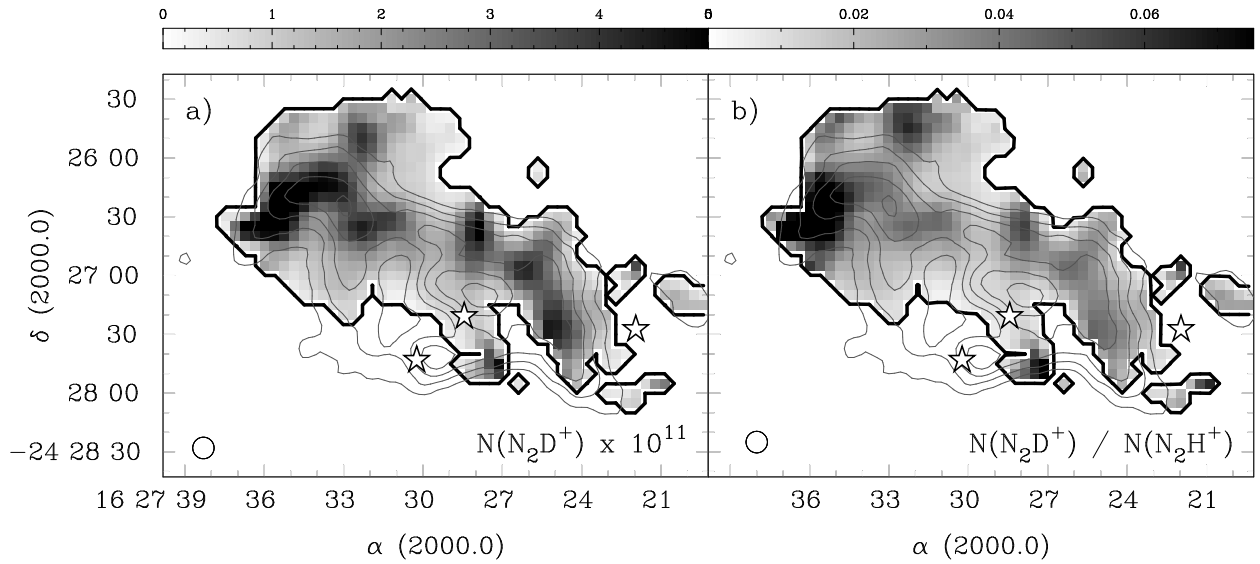


Fig. 7.— a) Total N_2D^+ column density $N(N_2D^+)$ (cm^{-2}) in Oph B2 determined using Equation 3 (greyscale). Values shown have been divided by 10^{11} . In both plots, only results from pixels where the S/N of the peak line intensity is ≥ 5 are shown, indicated by the thick black contour. Grey contours show $850 \mu m$ continuum emission as in Figure 5. The $18''$ (FWHM) beam is shown at lower left. Stars indicate the positions of Class I protostars. b) Fractional abundance of N_2D^+ relative to N_2H^+ , R_D , in Oph B2. The scale has been truncated to show the variation in central B2; the maximum $R_D = 0.16$ towards the eastern tip.

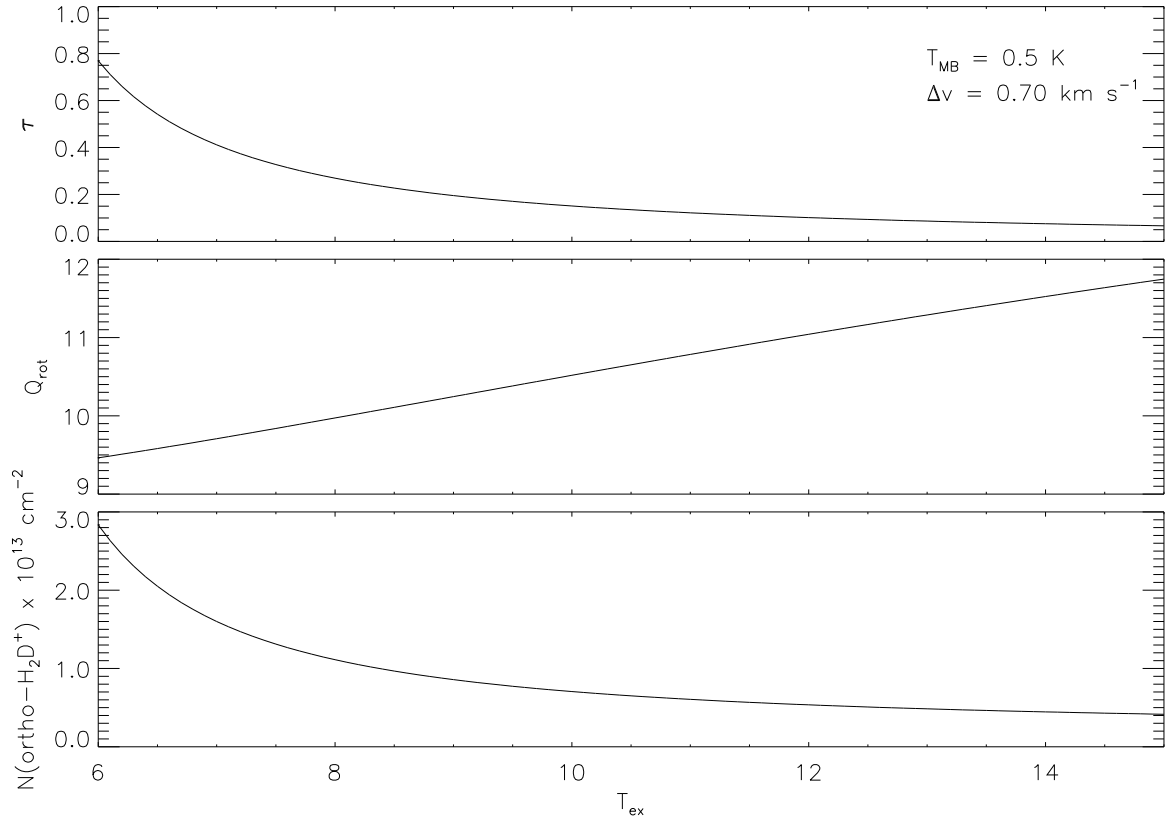


Fig. 8.— Impact of the assumed excitation temperature, T_{ex} , on returned H_2D^+ $1_{11} - 1_{10}$ line opacity (top), partition function Q_{rot} (middle), and column density, $N(\text{ortho-H}_2\text{D}^+)$, given a line brightness temperature T_{MB} and line width Δv similar to observed mean values in Oph B2. At low T_{ex} , τ and $N(\text{ortho-H}_2\text{D}^+)$ vary strongly with T_{ex} , but the effect of changes in T_{ex} at higher temperatures becomes small.

Table 3. Impact of T_{ex} on τ , Q_{rot} and $N(\text{ortho-H}_2\text{D}^+)$

T_{ex} K	τ	Q_{rot}	$N(\text{ortho-H}_2\text{D}^+)$ 10^{13} cm^{-2}
7	0.41	9.7	1.60
8	0.27	10.0	1.11
9	0.20	10.2	0.86
10	0.15	10.5	0.71
11	0.12	10.8	0.61
12	0.10	11.0	0.54
13	0.09	11.3	0.48
14	0.08	11.5	0.45
15	0.07	11.7	0.42

Note. — Values were calculated for a line strength $T_{MB} = 0.5 \text{ K}$ and width $\Delta v = 0.7 \text{ km s}^{-1}$.

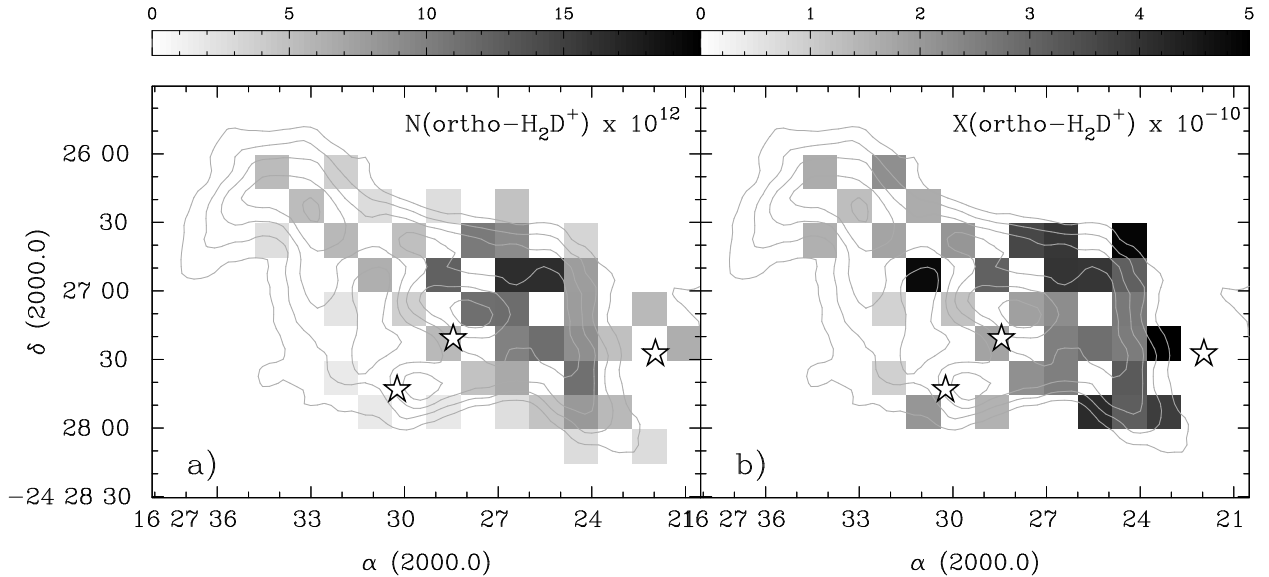


Fig. 9.— a) Ortho-H₂D⁺ column density in cm^{-2} (greyscale). $N(\text{ortho-H}_2\text{D}^+)$ values have been divided by 10^{12} . Grey contours show 850 μm continuum emission as in Figure 5. b) Fractional ortho-H₂D⁺ abundance $X(\text{ortho-H}_2\text{D}^+)$ (greyscale). Values have been divided by 10^{-10} .

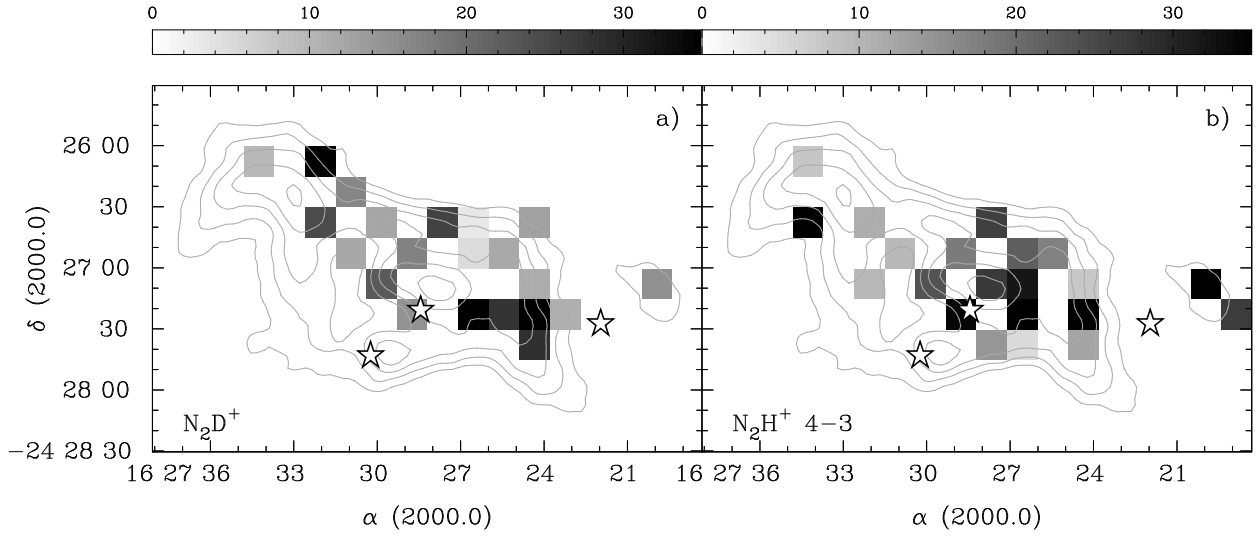


Fig. 10.— a) T_K determined using Equation 7 for H_2D^+ and N_2D^+ emission. Note that a negative T_K was found for the blank pixel towards the submillimetre continuum emission peak because the observed H_2D^+ $\Delta v > N_2D^+$ Δv . Grey contours show 850 μm continuum emission as in Figure 5. b) T_K determined using Equation 7 for H_2D^+ and N_2H^+ 4-3 emission.

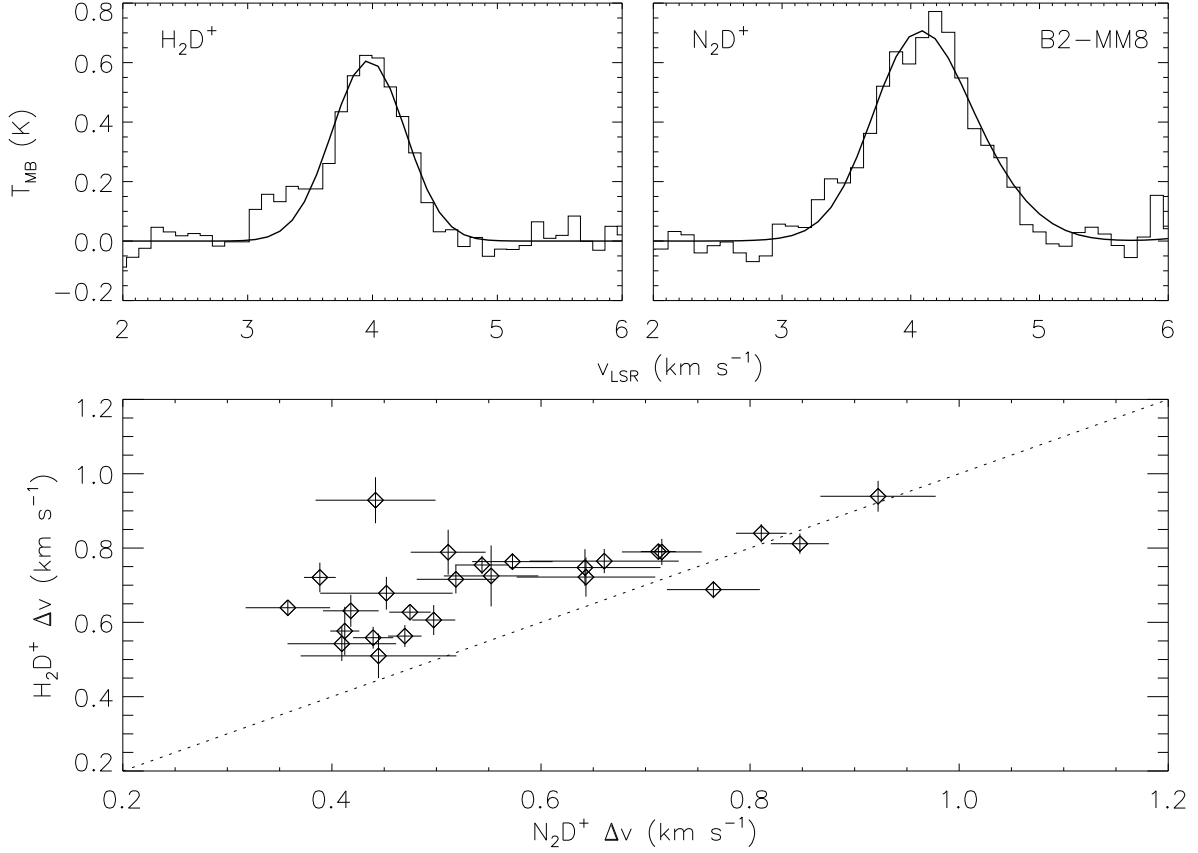


Fig. 11.— Top left: H_2D^+ $1_{11} - 1_{10}$ spectrum towards B2-MM8 overlaid with a Gaussian fit. Top right: N_2D^+ $3-2$ spectrum towards B2-MM8 overlaid with a hyperfine structure fit (note no individual hyperfine components are visible due to their small separation in velocity and the relatively large line width). Bottom: Returned H_2D^+ line widths Δv versus N_2D^+ Δv . Each point represents a $15''$ pixel. An equality relation is shown by the dotted line. Despite appearing wider, in most locations the N_2D^+ Δv is narrower than that of H_2D^+ due to the presence of overlapping hyperfine lines. The two points where N_2D^+ $\Delta v > \text{H}_2\text{D}^+$ Δv are located at and immediately adjacent to the $850 \mu\text{m}$ continuum peak and B2-MM8. At these locations, temperatures calculated via Equation 7 become negative and unphysical. Uncertainties shown are returned from the line fitting routines. Uncertainties in the line widths are shown.

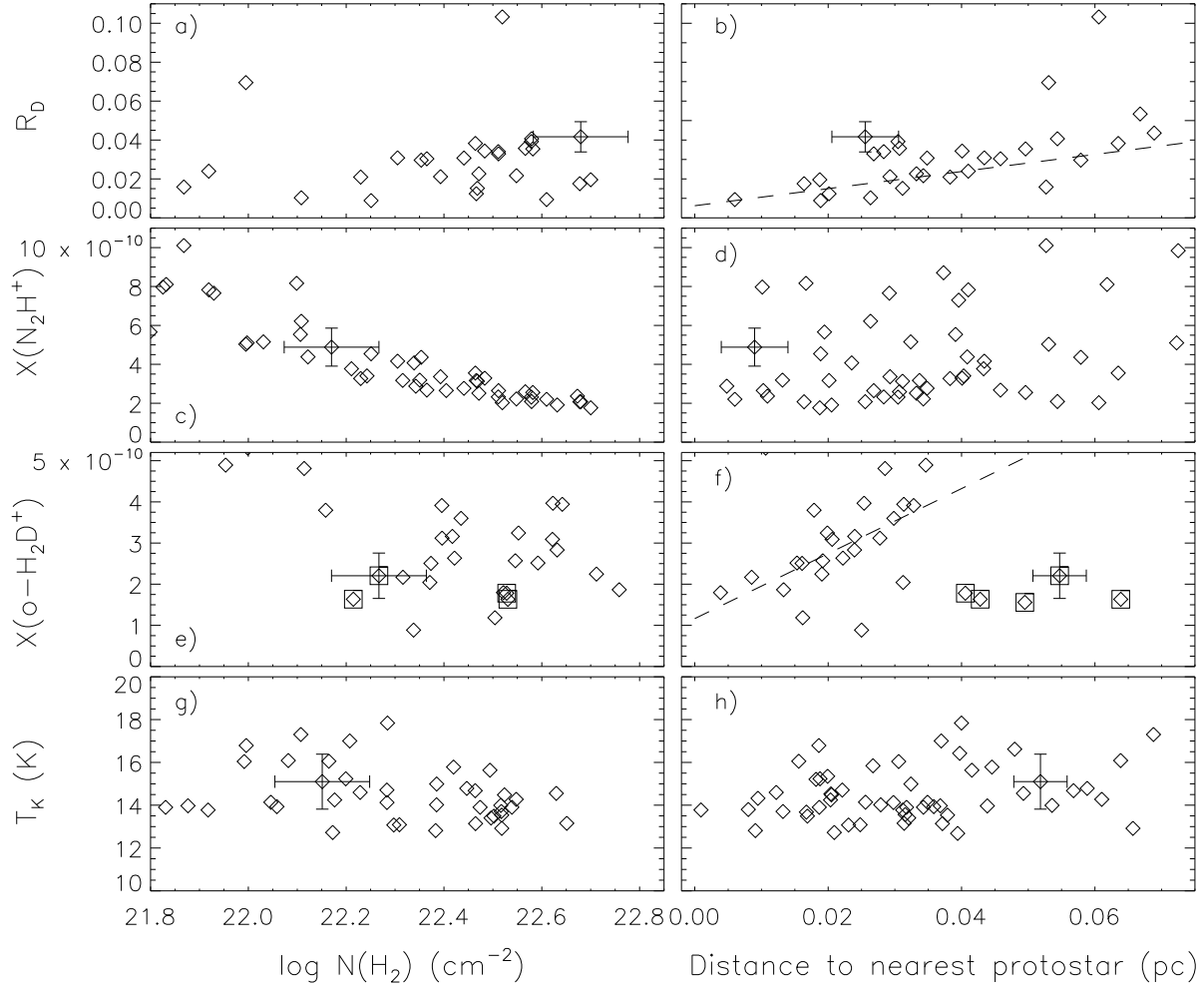


Fig. 12.— Variation in R_D , $X(\text{N}_2\text{H}^+)$, $X(\text{ortho-H}_2\text{D}^+)$ and T_K with H_2 column density and the projected distance to the nearest embedded protostar in Oph B2. In each plot, points shown represent pixels matched to the FWHM beam of the respective datasets ($15''$ for T_K and H_2D^+ , and $18''$ for N_2H^+ and N_2D^+). Typical uncertainties are shown for a single pixel in each plot. An uncertainty of $\sim 20 - 30\%$ in the $X(\text{ortho-H}_2\text{D}^+)$ values is not shown. Only pixels with $\text{S/N} > 5$ are plotted. In (a), no trend is found in R_D versus $\log N(\text{H}_2)$. The R_D data are, however, consistent with an increasing deuterium fractionation with distance from an embedded source (b), albeit with significant scatter. As discussed in Paper II, a strong correlation is seen in $X(\text{N}_2\text{H}^+)$ versus $\log N(\text{H}_2)$ (c), but no trend is seen with respect to projected protostellar distance (d). $X(\text{ortho-H}_2\text{D}^+)$ shows no trend with $\log N(\text{H}_2)$ (e). With respect to projected protostellar distance, the $X(\text{ortho-H}_2\text{D}^+)$ plot shows the data do not scatter about a central point (f), but instead show a trend of increasing $X(\text{H}_2\text{D}^+)$ to $d \sim 0.04$ pc, and a smaller, constant H_2D^+ abundance at further distances. In both (e) and (f), the points identified with squares represent pixels in the northeast portion of the B core. A linear fit to the data, omitting the highlighted pixels, is shown by the dotted line. A linear fit to the data is shown by the dashed line. No clear correlation is found in T_K versus $\log N(\text{H}_2)$ (g) or projected protostellar distance (h).